



# Identifying elastic wave polarization and bandgaps in periodic solid media

Maria Carrillo-Munoz, Bhisam Sharma\*

Department of Aerospace Engineering, Wichita State University, Wichita, KS 67260-042, USA

## ARTICLE INFO

### Keywords:

Elastodynamics  
Band gap  
Metamaterial  
Wave polarization  
Dispersion engineering

## ABSTRACT

We present a new computational method to accurately identify the elastic wave propagation modes and polarizations in periodic solid structures and metamaterials. The method uses the eigenvectors associated with each propagating wave solution to calculate the contribution of each translational and rotational component of the total mass-in-motion. We use this information to identify the dominant wave propagation mode by defining a relative effective modal mass vector. Then, we associate each wave solution with its correct polarization by defining a polarization factor that quantifies the relative orientation between the wave propagation and lattice motion directions and provides a positive numerical value between 0 (pure *S*-wave) and 1 (pure *P*-wave). Further, we suggest a graphical representational scheme for easier visualization of the wave polarization within traditional dispersion plots. To validate the method, we compare our predictions against previously published results for various elastodynamic problems. Finally, we use the proposed method to analyze the effect of various lattice and structural parameter perturbations on the elastic wave propagation and polarized bandgap behavior of a square planar beam lattice. Our analysis reveals the emergence of previously unobserved dynamic characteristics, including various polarized bandgaps, fluid-like behavior, and ultralow-frequency *SH*- and *SV*-bandgaps that extend to 0 Hz. Our proposed method provides an alternative computational approach to the typically employed visual mode inspection technique and provides a robust method for analyzing the elastic wave response of periodic solid media.

## 1. Introduction

Interest in phononic media and metamaterials stems from their novel bulk properties and from the possibility of controlling the flow of elastic energy through engineering structures [1–3]. Classically, research on these material systems has been focused on the emergence of wave attenuation bandgaps—frequency zones within which incident waves are spatially attenuated—as a function of their underlying substructure. In phononic media, this attenuation occurs because of substructural periodicity and the resultant Bragg scattering effects [1]; in metamaterials, the attenuation occurs due to localized substructural resonances sequestering the incident elastic energy [3,4]. While metamaterials do not strictly require a periodic substructure, this assumption is frequently made for the convenience of analysis and their eventual fabrication, leading to the appearance of both Bragg and local resonance attenuation effects [5–8].

The analysis of elastic wave propagation through such structures is mathematically complicated, vis-à-vis their photonic counterparts [4], because of the multiple wave modes or polarizations supported by

elastic media [9,10], their propensity to couple at higher frequencies [11–14], and their interconversion during reflections at the substructural interfaces [15–20]. Polarization is defined as the relative orientation between the wave propagation direction—conveniently described by the wave vector orientation—and the oscillation direction of the elastic particles [21,22]. An unbounded homogenous elastic medium supports the propagation of three uncoupled wave polarizations [23, 24]: one *P*-wave—also called dilatational, irrotational, longitudinal, compressional, voluminal, or primary (*P*) wave—wherein the particles oscillate parallel to the wave propagation direction; and two *S*-waves—also called distortional, equivoluminal, rotational, transversal, shear, or secondary (*S*) waves—wherein the particles oscillate perpendicular to the wave propagation direction. The two *S*-waves are further distinguished as *SH*- or *SV*-waves if the particle motion occurs in-plane (horizontal) or out-of-plane (vertical), respectively, relative to the plane defined by the particle oscillation, wave propagation direction, and the global coordinate choice. Heterogenous or anisotropic unbounded media support additional coupled waveforms with polarizations neither parallel nor perpendicular to the propagation direction

\* Corresponding author.

E-mail address: [bhisam.sharma@wichita.edu](mailto:bhisam.sharma@wichita.edu) (B. Sharma).

[24,25]. Depending on the dominant polarization, such coupled waves are classified as quasi- $P$  or quasi- $S$  waves; lacking a dominant polarization, such waves may be classified as hybrid [26]. Waveforms in bounded media are more commonly classified as longitudinal (equivalent to  $P$ -waves), flexural or bending or transverse (equivalent to  $SV$ -waves), shear (equivalent to  $SH$ -waves), and torsional waves where the particle motion comprises twisting or rotation about the propagation direction.

Depending on their underlying substructure—periodicity [8], property contrast ratios [27], symmetry [28,29], and connectedness [30,31] all play an important role—phononic media and metamaterials exhibit distinct bandgaps that can be either classified based on their generation mechanism as Bragg or local resonance bandgaps, as explained earlier, or based on the waveform types they attenuate. Polarized bandgaps [32,33] restrict the propagation of waves only with specific polarizations; for example, a  $P$ -wave bandgap only attenuates incident  $P$ -waves. The superposition of all polarized bandgaps within the same frequency range results in a complete or full bandgap within which all waves, irrespective of their polarization, are attenuated [32]. In multidimensional structures, the bandgaps can be further classified depending on their directional nature. Directional bandgaps [34–36] are frequency ranges where only waves propagating along specific directions are attenuated; waves with other incident angles or propagation directions propagate unattenuated through the structure. The overlap of such directional bandgaps along all  $4\pi$  radians results in absolute or omnidirectional bandgaps [37]. Thus, depending on their polarization and directionality, one may classify bandgaps as polarized-directional, polarized-omnidirectional, complete-directional, or complete-omnidirectional. Wave filtering, because of directional or polarized-directional bandgaps, forces incident waves to propagate in the other permitted directions [38,39]. This phenomenon has been harnessed by researchers to show the possibility of beaming or steering elastic waves along specific directions [35,36] and is also of interest for the inverse problem of non-destructively identifying damage by monitoring elastic energy flow [40,41]. Recently, researchers have also observed the appearance of polarization anomalies because of substructural heterogeneities [42–44], wherein the typically slower  $S$ -waves propagate faster than the  $P$ -waves.

These phenomena are traditionally studied by deriving the spectral or dispersion relations of the structure under consideration. Over the years, various analytical and numerical techniques have been used to obtain these relationships, including using equivalent spring-mass analogs [45], Hamiltonian energy method [46,47], space-harmonic method [48], receptance technique [49,50], transfer matrix method [5,51], phased array method [6,52], finite element method [36,53–56], plane wave expansion [57,58], and the spectral element method [59,60]. In general, these methods use a representative unit cell in conjunction with the Floquet-Bloch periodicity boundary condition to extract the wavenumber-frequency relationships of waves propagating through the global structure. While analytical methods become intractable as the substructural complexity increases, the finite element method provides a reliable route for analyzing such structures. Regardless of the method choice, the obtained spectral curves or surfaces provide information about the dispersion behavior of the propagating waves. Omnidirectional and complete bandgaps are then easily identified as frequency regions with no real-valued solutions. However, associating each dispersion curve or surface with its polarization and consequently identifying individual polarized and polarized-directional bandgaps requires further analysis. These polarized bandgaps are most frequently identified by observing the mode shapes at the bandgap edge frequencies at the high-symmetry irreducible Brillouin zone (IBZ) points [31–33]. While this is easily done at lower frequencies where the wave polarizations are usually uncoupled, manually identifying the polarizations gets complicated for coupled waves. Further, curve veering [12, 13,61]—described by Manconi and Mace [12] as a phenomenon where “two or more eigenvalue loci of a system with a varying parameter veer away and diverge instead of crossing”—and the possible continuous variation of

polarization as the wave vector sweeps the IBZ [22], further complicate the accurate wave polarization identification using mode shape observation at high-symmetry points. Some researchers have employed alternative methods to identify polarizations. Focusing on sagittal acoustic waves, Manzanares-Martinez and Ramos-Mendieta [22] adopted a strain energy balance approach and obtained the averaged longitudinal and transversal displacement contributions for one-dimensional phononic crystal unit cells; for two-dimensional cases, the authors avoid defining a local wave vector by instead calculating the average compression and shear contributions and approximating them to longitudinal and transversal vibrations. Similarly, Achaoui et al. [62] used the integrals of displacement field components as representative of wave polarization without considering the wave vector direction. A different approach, accounting for the wave vector direction, was adopted recently by Bacigalupo and Lepidi [26], who proposed a family of non-dimensional polarization factors to quantify the wave polarization and energy flow in periodic beam lattice materials and showed the coincidence between the energy and group velocities. To predict out-of-plane wave beaming in two-dimensional lattices, Zelhofer and Kochmann [36] distinguished the in-plane and out-of-plane wave modes using a scalar in-plane ratio calculated using the mass normalized eigenvectors. Lee et al. [43] identified the polarization characteristics of a double-slit metamaterial showing polarization anomalies by calculating the absolute value of the relative angle between the polarization orientation and the wave vector orientation.

In this work, we propose a systematic approach to identify wave propagation modes and to accurately associate the dispersion curves with their respective polarizations. We adapt the concept of the modal participation factor [63,64], commonly used in vibration modal analysis, to quantify the relative participation of each directional motion component to the wave mode associated with each dispersion solution. We then calculate the relative orientation between the wave propagation and particle motion directions by defining a polarization factor which provides a positive numerical value between 0 and 1, where 0 indicates a pure  $S$ -wave, 1 indicates a pure  $P$ -wave, and the interim values indicate quasi- or hybrid polarizations. Further, we suggest a graphical representational scheme for the easier visualization of the wave polarizations within traditional dispersion plots. Though our focus here is on utilizing existing eigenvector data that is calculated during the numerical calculation of the dispersion curves, the method is easily adaptable for use with other techniques that provide eigenvector data. The novelty of the proposed method lies in its ability to clearly elucidate the wave propagation mode and polarizations underlying each dispersion solution; this clarity enables the identification of previously unobserved emergent behaviors in widely studied lattice geometries.

## 2. Background and motivation

In this section, we provide a detailed background on the computational method used to obtain the elastic wave dispersion curves of periodic structures. Specifically, we describe the numerical approach for calculating dispersion solutions of periodic structures by applying Floquet-Bloch boundary conditions on a representative unit cell and extracting eigenfrequency solutions corresponding to specific wave vectors. We then use the example of an infinite, planar square beam lattice to illustrate the need for a new approach to identify the wave propagation modes and polarizations by demonstrating the errors that can result from the currently used visual mode shape inspection method.

### 2.1. Elastic wave dispersion relations

The propagation behavior of elastic waves in phononic structures and metamaterials with substructural periodicity is conveniently studied by applying Floquet-Bloch boundary conditions on a representative unit cell. The time-harmonic displacement field within an infinite periodic structure can be represented as:

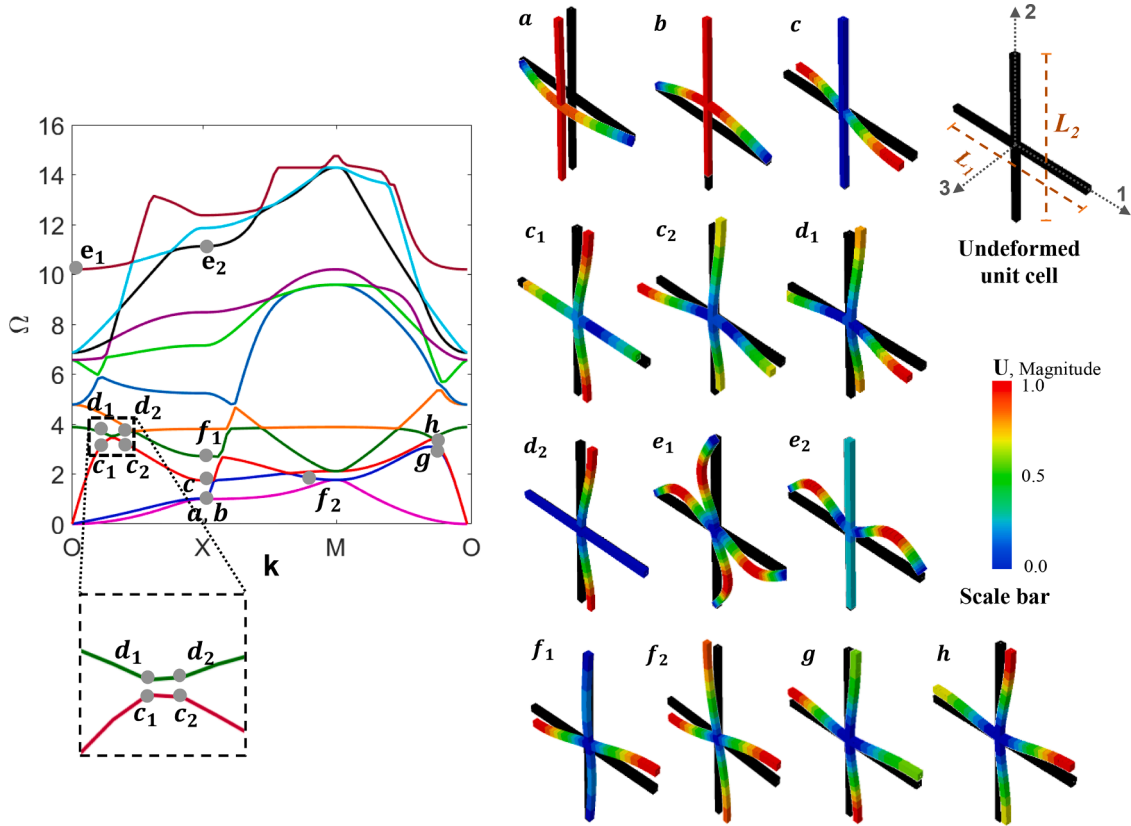


Fig. 1. Dispersion curves for a square beam lattice with six degrees-of-freedom and the unit cell mode shapes at the specified dispersion points. The inset shows the curve veering phenomena occurring between the 3rd and 4th eigenfrequency curves.

$$u_A(r, t) = U_A(r) e^{-i\omega t}, \quad (1)$$

where  $U_A$  is the complex displacement amplitude at point  $A$  with a position vector  $r$ ,  $t$  is the time variable,  $\omega$  is the wave frequency, and  $i = \sqrt{-1}$ . According to Floquet-Bloch theory, the response at any point  $A$  in a periodic structure is related to the response at the corresponding spatially periodic point  $A'$  with position vector  $r'$  through the complex wave vector  $k$  as:

$$U_{A'}(r') = U_A(r) e^{-ik(r'-r)} \quad (2)$$

In this representation, the real component of the complex wave-number is the phase difference between points  $A$  and  $A'$ , the imaginary component—also called the wave attenuation factor—is the decay rate of the wave amplitude between the two points, and the wave vector direction indicates the propagation direction of the elastic waves. For non-dissipative linear materials,  $k$  is purely real for the propagating waves and becomes purely imaginary within wave attenuation bandgaps: frequency regions where waves are spatially attenuated and do not propagate through the structure. The dispersion behavior of the propagating waves and the existence of bandgaps is studied by applying Floquet-Bloch boundary condition on the unit cell and then calculating the eigenfrequency solutions while sweeping over the wave vectors of interest. This approach, frequently referred to as the  $\omega(k)$  approach, leverages the theorem that a structure which is periodic in the physical space with a periodicity  $L$  is also periodic in the wave vector space—also called the reciprocal space—with periodicity  $2\pi/L$ . Thus, a unit cell with periodicity  $L_1$ ,  $L_2$ , and  $L_3$  along the 1-, 2-, and 3-axis results in a reciprocal space with wavenumber periodicity  $k_1 \rightarrow 2\pi/L_1$ ,  $k_2 \rightarrow 2\pi/L_2$ , and  $k_3 \rightarrow 2\pi/L_3$ . The unit cell representing this resultant reciprocal space is called the Brillouin zone. By choosing the reciprocal unit cell to be centered around the point  $k = 0$  and allowing only positive  $k$  values, we can reduce the computational wave vector domain to  $k_1 \rightarrow [0, \pi/L_1]$ ,  $k_2$

$\rightarrow [0, \pi/L_2]$ , and  $k_3 \rightarrow [0, \pi/L_3]$ . This reduced domain—called the First Brillouin Zone—can be shrunk further by exploiting its symmetry to get the Irreducible Brillouin Zone (IBZ). As the name suggests, the IBZ is the smallest possible reciprocal unit cell which provides complete information about a periodic structure's spectral behavior. Thus, the  $\omega(k)$  approach involves sweeping over the IBZ while solving for the real-only frequencies allowed by the structure.

For complicated geometries, the above technique is frequently implemented using the finite element (FE) method, where the unit cell is modeled using an appropriate mesh and the boundary nodes are constrained using Eq. (2). While some commercial FE software (e.g., Comsol Multiphysics) allow the direct application of complex-valued boundary conditions, others (e.g., Abaqus CAE) only allow the application of real-valued displacements. Åberg and Gudmundson [55] showed that this limitation can be overcome by separating the model into two identical 'real' and 'imaginary' mesh parts and by formulating the total complex-valued displacement at a lattice point  $A$  as:

$$U_A = U_{A_{re}} + i U_{A_{im}} \quad (3)$$

where  $U_{A_{re}}$  and  $U_{A_{im}}$  are the displacements of the corresponding nodes at point  $A$  of the real and imaginary models, respectively. Then, the complex Floquet-Bloch boundary conditions in Eq. (2) are implemented by applying Euler's equation to get:

$$U_{A'_{re}} = U_{A_{re}} \cos(k(r' - r)) + U_{A_{im}} \sin(k(r' - r)) \quad (4)$$

$$U_{A'_{im}} = U_{A_{re}} (-\sin(k(r' - r))) + U_{A_{im}} \cos(k(r' - r)) \quad (5)$$

The eigenfrequencies corresponding to the wave vector values within the IBZ are then extracted using a linear perturbation analysis procedure. The equations of motion for the free vibration of the unit cell with boundary nodes constrained using Eq. (4) and Eq. (5) are:

$$M\ddot{u} + Ku = 0 \quad (6)$$

where  $u$  and  $\ddot{u}$  are the displacement and acceleration vectors, with  $\ddot{u}$  signifying two time derivatives of  $u$ , and  $M$  and  $K$  are the global mass and stiffness matrices, respectively. Assuming the solution to be the time-harmonic displacement field given in Eq. (1) leads to the eigenvalue problem:

$$(K - \omega^2 M)U = 0 \quad (7)$$

By introducing a constraint matrix  $Q$ , the equations can be rewritten in terms of the displacements of the unconstrained internal nodes,  $U_{\text{int}}$ , and the master boundary nodes,  $U_{\text{bdry}}$ , as:

$$\begin{bmatrix} U_{\text{intre}} \\ U_{\text{bdryre}} \cos(k(r' - r)) + U_{\text{bdryim}} \sin(k(r' - r)) \\ U_{\text{bdryre}} \\ U_{\text{intim}} \\ U_{\text{bdryre}} (-\sin(k(r' - r))) + U_{\text{bdryim}} \cos(k(r' - r)) \\ U_{\text{bdryim}} \end{bmatrix} = Q \begin{bmatrix} U_{\text{intre}} \\ U_{\text{bdryre}} \\ U_{\text{intim}} \\ U_{\text{bdryim}} \end{bmatrix} \quad (8)$$

where the matrix  $Q$  is defined as:

$$Q = \begin{bmatrix} I & 0 & 0 & 0 \\ 0 & \cos(k(r' - r)) & 0 & \sin(k(r' - r)) \\ 0 & 0 & I & 0 \\ 0 & 0 & 0 & I \\ 0 & -\sin(k(r' - r)) & 0 & \cos(k(r' - r)) \\ 0 & 0 & 0 & 0 \end{bmatrix} \quad (9)$$

The resulting eigenvalue problem is a function of the wave vector and is given as:

$$\left( \begin{bmatrix} K & 0 \\ 0 & K \end{bmatrix} - \omega^2 \begin{bmatrix} M & 0 \\ 0 & M \end{bmatrix} \right) Q \begin{bmatrix} U_{\text{intre}} \\ U_{\text{bdryre}} \\ U_{\text{intim}} \\ U_{\text{bdryim}} \end{bmatrix} = \begin{bmatrix} 0 \\ 0 \\ 0 \\ 0 \end{bmatrix} \quad (10)$$

Solving this equation provides the eigenfrequency solutions corresponding to the specific wave vectors. The graphical representation of these solutions as  $\omega$  v/s  $k$  plots provides a clearer understanding of the structure's dispersion behavior and the presence of bandgaps. For a general three-dimensional case, the solutions can be plotted for the entire IBZ volume to obtain the dispersion volumes; plotting over a two-dimensional grid covering the two-dimensional IBZ provides dispersion surfaces; plotting along a one-dimensional path—typically chosen to traverse the IBZ boundaries—provides dispersion curves. The obtained information can be further processed to calculate the group and phase velocities and to study the structure's wave directionality behavior [34–36,65].

## 2.2. Elastic wave polarization

As an illustrative example, consider the dispersion plot for an infinite, planar square beam lattice, as shown in Fig. 1, with six degrees-of-freedom, obtained using the procedure described in Section 2.1. We model the lattice in Abaqus CAE as an interconnected network of three-dimensional deformable wires, meshed using the shear-flexible beam elements with quadratic interpolation (B32). We assume that the unit cell lies in the  $I$ - $2$  plane and that its lattice constants along the  $I$ - and  $2$ -axis are  $L_1 = 1$  m and  $L_2 = 1$  m, respectively. The lattice elements are assumed to have a square cross-section of 77 mm thickness. The dispersion curves obtained along the IBZ path O-X-M-O are shown in Fig. 1, where we normalize the frequency axis with respect to the frequency of the first in-plane bending mode occurring at the high-

symmetry point X ( $k_1 = \pi/L_1$ ,  $k_2 = 0$ ). The mode shapes at specific dispersion point locations are also shown

Each continuous eigenfrequency curve in the dispersion plots, shown here using different colors, represents a solution to Eq. (6); each eigenfrequency represents a specific permitted wave propagation mode or polarization at that frequency. However, each continuous curve does *not* correspond to a single propagation mode; one must also pay attention to the associated eigenvectors to determine this information. Traditionally, the associated polarizations are identified by visually inspecting the mode shapes at each eigenfrequency; to identify the attenuation bandgaps, attention is usually restricted to the bandgap start and stop eigenfrequencies [32,66]. For example, the mode shapes at the points  $a$ ,  $b$ , and  $c$  along the high-symmetry point X show that their associated eigenfrequency curves, shown here in pink, blue, and red, respectively, are the propagating wave solutions for the first SV-, first SH-, and second SV-waves, respectively. However, further inspection of the mode shapes at points  $c_1$  and  $c_2$  along the third eigenfrequency (red) curve shows that while point  $c_2$  is indeed the second SV-wave, point  $c_1$  is a P-wave mode. This polarization change occurs because of the curve or mode veering phenomena [12,13,67] shown in the inset, where the dispersion curves associated with the P- and SV-waves abruptly switch polarizations and veer away and diverge instead of crossing over each other. Here, the eigenfrequency curves containing points  $c_1$  and  $c_2$ , and the points  $d_1$  and  $d_2$  switch polarizations, as seen in the similarity of the mode shapes at points  $c_1$  and  $d_2$ , and points  $c_2$  and  $d_1$ . Such curve veering effects can lead to the incorrect identification of the wave polarizations associated with each dispersion curve. Another source of error in the visual mode shape inspection approach stems from the mode conversion effects, where the polarization associated with a single dispersion curve might vary continuously as a function of the wave vector [22]. For the square lattice, such mode conversion effects are seen in the 11th dispersion curve along O-X: the curve starts ( $e_1$ ) as a hybrid wave mode with similar contributions by the in-plane flexural motion in the vertical (P-mode) and horizontal (SH-mode) lattice elements but slowly converts to an SH-wave mode, where the horizontal element's in-plane flexural motion is the dominant response, as seen at point  $e_2$ . A similar mode conversion occurs in the 3rd dispersion curve along the X-M path: the curve begins at point  $f_1$  with horizontal element dominated flexural motion along the 2-direction and gradually converts to a hybrid mode with in-plane flexural motion of the horizontal and vertical elements along the 2- and 1-directions, respectively. Besides the mode veering and conversion effects, the coupled mode shapes underlying the waves propagating in directions unaligned with lattice element orientations, as seen at point  $g$ , further complicate the accurate identification of the wave polarizations. Consequently, while the complete and omnidirectional bandgaps are easily identified as frequency regions with no real eigen solutions, relying on visual mode shape inspection can easily result in the misidentification of polarized bandgaps.

## 3. Method

In this section, we present a new method for associating the dispersion curves with their respective polarizations. For a FE mesh, every eigenfrequency is associated with an eigenvector at each node. The proposed method uses these eigenvectors to calculate the relative effective translational and rotational masses-in-motion along the different coordinate directions at each eigenfrequency. This information is then used to identify the structural vibration mode associated with the wave propagation at each frequency. While this is sufficient for the correct polarization identification of waves with wave vectors oriented along the structural elements, we propose the use of a polarization factor to ensure the accurate polarization identification of waves with different wave vector orientations. Finally, we present a visualization scheme to allow the easier identification of various wave modes and polarized bandgaps.

**Table 1**

The calculated modal effective mass vectors, relative effective modal mass vectors, and the identified propagation mode for the specific points shown in Fig. 1.

Location	Normalized frequency $\Omega^n$	Modal effective mass vectors $m_{\text{eff}}^n$	Relative effective translational mass $q_t^n = (q_{t_1}^n, q_{t_2}^n, q_{t_3}^n)$	Relative effective rotational mass $q_r^n = (q_{r_4}^n, q_{r_5}^n, q_{r_6}^n)$	Propagation mode
$c_1$	3.41	(14.4, 0, 0, 0, 0, 0)	(1, 0, 0)	(0.035, 0.996, 0.004)	In-plane
$c_2$	3.40	(0, 0, 0.183, 0, 0.292, 0)	(0, 0, 1)	(0, 1, 0)	Out-of-plane
$d_1$	3.47	(0, 0, 0.125, 0, 0.246, 0)	(0, 0, 1)	(0, 1, 0)	Out-of-plane
$d_2$	3.49	(13.2, 0, 0, 0, 0, 0)	(1, 0, 0)	(0, 0.994, 0.0057)	In-plane
$g$	2.98	(7.21, 7.21, 0, 0, 0, 0.297)	(0.5, 0.5, 0)	(0, 0, 1)	In-plane
$h$	3.19	(8.31, 8.31, 0, 0, 0, 0)	(0.5, 0.5, 0)	(0.195, 0.038, 0.767)	In-plane

### 3.1. Propagation mode identification

The method described in Section 2.1 provides the eigenfrequencies corresponding to the specific wave vectors of interest. Each eigenfrequency in the  $n^{\text{th}}$  dispersion curve,  $\omega^n$ , is associated with an eigenvector,  $U^n$ , at each FE node. The six eigenvector components  $U_j^n | j = 1, 2, \dots, 6$ —where  $U_j^n | j = 1, 2, 3$  are associated with the three translational components  $u_1^n, u_2^n, u_3^n$  along the 1, 2, and 3 coordinate directions, respectively, and  $U_j^n | j = 4, 5, 6$  are associated with the three rotational components  $\theta_1^n, \theta_2^n, \theta_3^n$  about the 1, 2, and 3 coordinate directions, respectively—provide information about the relative motion of each FE node at  $\omega^n$ . The relative influence of each eigenvector component on the overall mode shape can be estimated by calculating the associated modal participation factor,  $\Gamma^n$ , defined as:

$$\Gamma^n = \frac{U^{nT} M R}{m^n} \tag{11}$$

where  $M$  is the global mass matrix, and  $R$  and  $m^n$  are the influence matrix and generalized mass, defined respectively as:

$$R = \begin{pmatrix} 1 & 0 & 0 & 0 & (z - z_0) & -(y - y_0) \\ 0 & 1 & 0 & -(z - z_0) & 0 & (x - x_0) \\ 0 & 0 & 1 & (y - y_0) & -(x - x_0) & 0 \\ 0 & 0 & 0 & 1 & 0 & 0 \\ 0 & 0 & 0 & 0 & 1 & 0 \\ 0 & 0 & 0 & 0 & 0 & 1 \end{pmatrix} \tag{12}$$

$$m^n = U^{nT} M U^n \tag{13}$$

Here,  $R$ , represents the displacements resulting from any static unit ground displacement or rotation, where  $x, y, z$  are the nodal coordinate components, and  $x_0, y_0, z_0$  are the coordinates of the center of rotation along the 1-, 2-, and 3-axis, respectively. Note that by defining it this way,  $R$  degenerates into the identity matrix when the center of rotation coincides with the center of gravity.

While the modal participation factor is routinely used during modal analysis to understand the participation of individual normal modes to the overall dynamic state of a structure at a given frequency [63,64, 68–70], here, we propose using it to understand the relative participation of each directional motion component to the mode shape associated with a given eigenfrequency. Thus, the modal participation factor component  $\Gamma_j^n$  describes the contribution of the  $j^{\text{th}}$  directional motion component to the overall mode shape at  $\omega^n$ . The modal participation factor can then be used to quantify the portion of the translational ( $j = 1, 2, 3$ ) or rotational ( $j = 4, 5, 6$ ) mass along each direction by calculating the modal effective mass as:

$$m_{\text{eff}}^n = \Gamma^{n2} m^n \tag{14}$$

For convenience of comparison, we normalize the translational and rotational effective mass components as:

$$c_j^n = \frac{m_{\text{eff}}^n j}{M}, \text{ for } j = 1, 2, \text{ and } 3 \text{ (translational mass)} \tag{15}$$

$$c_j^n = \frac{m_{\text{eff}}^n j}{I_j}, \text{ for } j = 4, 5, \text{ and } 6 \text{ (rotational mass)} \tag{16}$$

where  $M$  and  $I_j$  are the total translational and rotational mass of the structure. Note that while the translational mass is direction independent, the rotational mass (or moment of inertia) is directionally dependent and must be calculated about the appropriate axis. To better visualize the relative contribution of each effective mass component to the overall modal mass at  $\omega^n$ , we further normalize them with respect to the total translational and rotational effective masses as:

$$q_{t_j}^n |_{j=1,2,3} = \frac{c_j^n}{\sum_{j=1}^3 c_j^n} \tag{17}$$

$$q_{r_j}^n |_{j=4,5,6} = \frac{c_j^n}{\sum_{j=3}^6 c_j^n} \tag{18}$$

where  $q_{t_j}^n$  and  $q_{r_j}^n$  are the relative effective translational and rotational mass components along the  $j^{\text{th}}$  direction at  $\omega^n$ , respectively. This additional normalization provides relative effective mass component values bounded between 0 and 1, where 0 indicates no mass motion along that coordinate direction and 1 indicates that all the mass is moving in that direction. Note that the eigenvectors, modal participation factor, and the unnormalized modal effective mass components associated with each eigenfrequency can be directly extracted from most FE packages, including Abaqus CAE and Comsol Multiphysics. Further normalization of the modal effective mass components to calculate the relative effective translational and rotational mass components can be performed using any mathematical software; in this study, all calculations were performed using Matlab.

For clarity, reconsider locations  $c_1, c_2, d_1$ , and  $d_2$  in the 3rd and 4th dispersion curves for the square planar lattice shown in Fig. 1 as an example. The wave vector direction for all four points is along the 1-axis. The modal effective mass vectors and the relative effective modal mass vectors for these four points calculated using the above procedure are given in Table 1, where  $\omega^n$  is the frequency and  $\Omega^n$  is the normalized frequency of each location. At  $c_1$  and  $d_2$ , the dominant motion of the structural mass, as predicted by the modal mass vectors, is primarily the in-plane displacement along the 1-axis; conversely, the motion at  $c_2$  and  $d_1$  is dominated by displacement along 3-axis—i.e., out-of-plane—and rotation about the 2-axis, indicating that both these points are associated with the out-of-plane propagation mode. These predictions, verified by observing the mode shapes provided in Fig. 1, help in identifying the correct propagation mode at these four points that are affected by the curve veering phenomena. Similarly, the motion at locations  $g$  and  $h$ , studied further in Section 3.2, are also identified as in-plane. The modal effective mass vectors and the relative effective modal mass vectors for all locations shown in Fig. 1 are provided in the Appendix, Table A1.

### 3.2. Polarization identification

As defined previously, wave polarization is the relative orientation between the oscillation direction of the elastic particles and the wave

**Table 2**

The calculated translational modal participation factor, local wave vector orientation, polarization factor, and the identified wave polarization.

Location	Normalized frequency $\Omega^n$	Translational components of the modal participation factor $\Gamma_t^n$	Local wave vector $k_d$	Polarization factor $\Phi^n$	Wave polarization
$c_1$	3.4128	$\langle 1.83, 0, 0 \rangle$	$\langle 1, 0, 0 \rangle$	1	<i>P</i> -wave
$c_2$	3.4037	$\langle 0, 0, -0.1160 \rangle$	$\langle 1, 0, 0 \rangle$	0	<i>SV</i> -wave
$d_1$	3.4771	$\langle 0, 0, -0.15 \rangle$	$\langle 1, 0, 0 \rangle$	0	<i>SV</i> -wave
$d_2$	3.4954	$\langle 1.35, 0, 0 \rangle$	$\langle 1, 0, 0 \rangle$	1	<i>P</i> -wave
$g$	2.9817	$\langle 0.497, -0.497, 0 \rangle$	$\langle -1, -1, 0 \rangle$	0	<i>SH</i> -wave
$h$	3.1927	$\langle 0.566, 0.566, 0 \rangle$	$\langle -1, -1, 0 \rangle$	1	<i>P</i> -wave

vector. While the wave vector direction is known a priori, the oscillation direction is captured by the modal participation factor,  $\Gamma^n$ , which quantifies the contribution of each directional motion component to the mode shape at any given eigenfrequency. Thus, the relative orientation between the two vectors can be calculated using a polarization factor,  $\Phi^n$ , defined as:

$$\Phi^n = |\cos\varphi^n| \tag{19}$$

where

$$\cos\varphi^n = \frac{\langle \Gamma_t^n, k_d \rangle}{\|\Gamma_t^n\| \|k_d\|} \tag{20}$$

Here,  $\Gamma_t^n$  and  $k_d$  are the translational components of the modal participation factor and the local reciprocal lattice vector, and are given as:

$$\Gamma_t^n = \langle \Gamma_1^n, \Gamma_2^n, \Gamma_3^n \rangle \tag{21}$$

$$k_d = \langle \Delta k_1, \Delta k_2, \Delta k_3 \rangle \tag{22}$$

where,  $\Delta k_1, \Delta k_2, \Delta k_3$  are the increments of the wave vector components along the 1-, 2- and 3-axis, respectively.

The polarization factor provides a positive numerical value between 0 and 1, quantifying the relative angle between the wave propagation and lattice motion directions: 0 means that the oscillation is perpendicular to the wave propagation direction—indicating a *S*-wave; 1 means that the oscillation is parallel to the wave propagation direction—indicating a *P*-wave. For cases without pure polarizations, one may use the nomenclature ‘quasi-*S*’ if the polarization factor is less than 0.1, and ‘quasi-*P*’ if it is greater than 0.9; waves with polarization values in between these bounds may be classified as ‘hybrid’ waves.

For clarity, reconsider the locations  $c_1, c_2, d_1,$  and  $d_2$  in Fig. 1 and as discussed above. The calculated modal participation factor, local reciprocal lattice vector, and polarization factor are given in Table 2. The polarization factors at locations  $c_1$  and  $d_2$  reveal that the oscillation

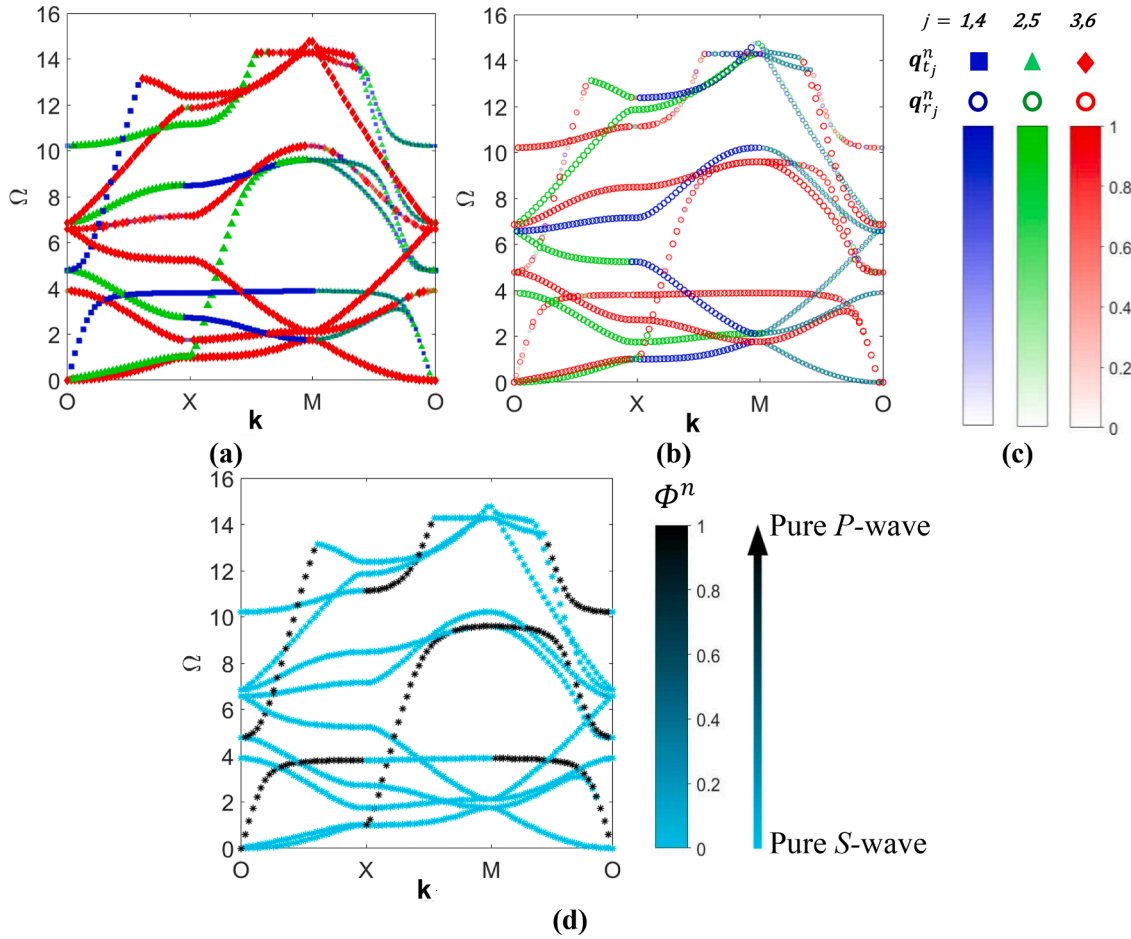
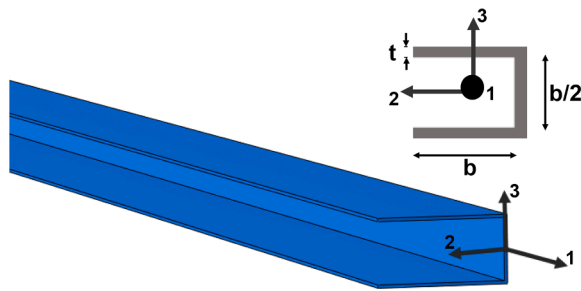


**Fig. 2.** Dispersion curves with overlaid relative effective modal mass vector components. Fig. 2(a) shows the translational components, Fig. 2(b) shows the rotational components, and Fig. 2(c) shows the color scales and symbols used for each component. Fig. 2(d) shows the polarization plot and the color scale used to identify the different polarization values.



Elastic modulus = 68.95 GPa  
 Poisson's ratio = 0.32  
 Density = 2600 kg/m<sup>3</sup>  
 Beam length = 1.016 m  
 b = 2.54 cm  
 t = 63.5 mm

Fig. 3. The analyzed thin-walled cantilever beam with an open, symmetric channel cross-section. The figure shows the geometrical and material properties used by Noor et al. [71].

direction of the structure at both locations is parallel to the wave propagation direction, thus correctly identifying the eigenfrequency at these locations as a *P*-wave solution. Similarly, the polarization factors at *c*<sub>2</sub> and *d*<sub>1</sub> correctly identify these locations as an *S*-wave solution; since the dominant motion for both these locations is along the out-of-plane axis, as shown in Table 1, the propagation mode can be further distinguished as an *SV*-wave solution.

The necessity of calculating the polarization factor is reinforced by considering points *g* and *h*—both are at the same wave vectors but at different frequencies. Identifying the polarizations of such locations is typically complicated since the wave vector is not oriented along a lattice element. As seen in Table 2, their polarization factors reveal that while oscillation direction at location *g* is perpendicular to the propagating wave direction, the oscillation direction at location *h* is parallel to the wave direction. Thus, the eigenfrequencies at locations *g* and *h* must be classified as *SH*- and *P*-waves, respectively. The calculated modal participation factors, local reciprocal lattice vectors, and polarization

factors for all locations shown in Fig. 1 are provided in the Appendix, Table A2.

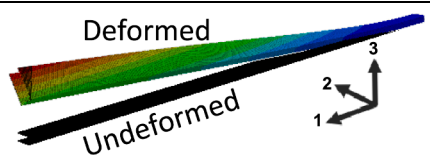
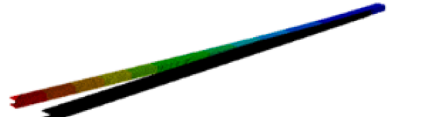
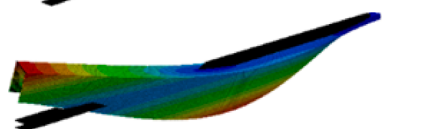
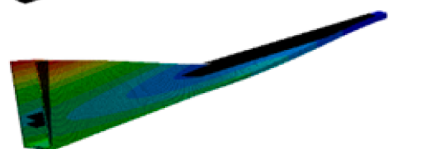
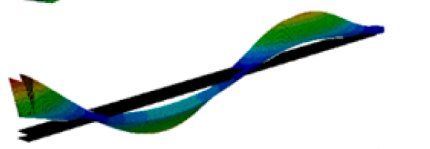
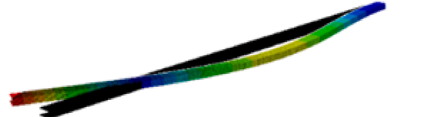
### 3.3. Visualization schema

For easier visualization of the contribution of each relative effective modal mass vector component to the overall motion of the structure at any given eigenfrequency solution, we represent each individual component using the following color scheme:

- $q_{t_1}^n \rightarrow$  solid blue squares
- $q_{t_2}^n \rightarrow$  solid green triangles
- $q_{t_3}^n \rightarrow$  solid red diamonds
- $q_{r_1}^n \rightarrow$  hollow blue circles
- $q_{r_2}^n \rightarrow$  hollow green circles
- $q_{r_3}^n \rightarrow$  hollow red circles

Table 3

The first six natural frequencies, relative effective mass vector components, and the mode shapes obtained from the FE solver.

Mode number <i>n</i>	Natural frequency $\omega^n$ (Hz)	Relative effective translational mass $\mathbf{q}_t^n = \langle q_{t_1}^n, q_{t_2}^n, q_{t_3}^n \rangle$	Relative effective rotational mass $\mathbf{q}_r^n = \langle q_{r_1}^n, q_{r_2}^n, q_{r_3}^n \rangle$	Deformed and undeformed mode shapes
1	11.43	$\langle 0, 0, 1 \rangle$	$\langle 0.372, 0.628, 0 \rangle$	
2	23.158	$\langle 0, 1, 0 \rangle$	$\langle 0, 0, 1 \rangle$	
3	42.705	$\langle 0, 0, 1 \rangle$	$\langle 0.656, 0.344, 0 \rangle$	
4	57.925	$\langle 0, 0, 1 \rangle$	$\langle 0.624, 0.376, 0 \rangle$	
5	106.96	$\langle 0, 0, 1 \rangle$	$\langle 0.212, 0.788, 0 \rangle$	
6	144.5	$\langle 0, 1, 0 \rangle$	$\langle 0, 0, 1 \rangle$	

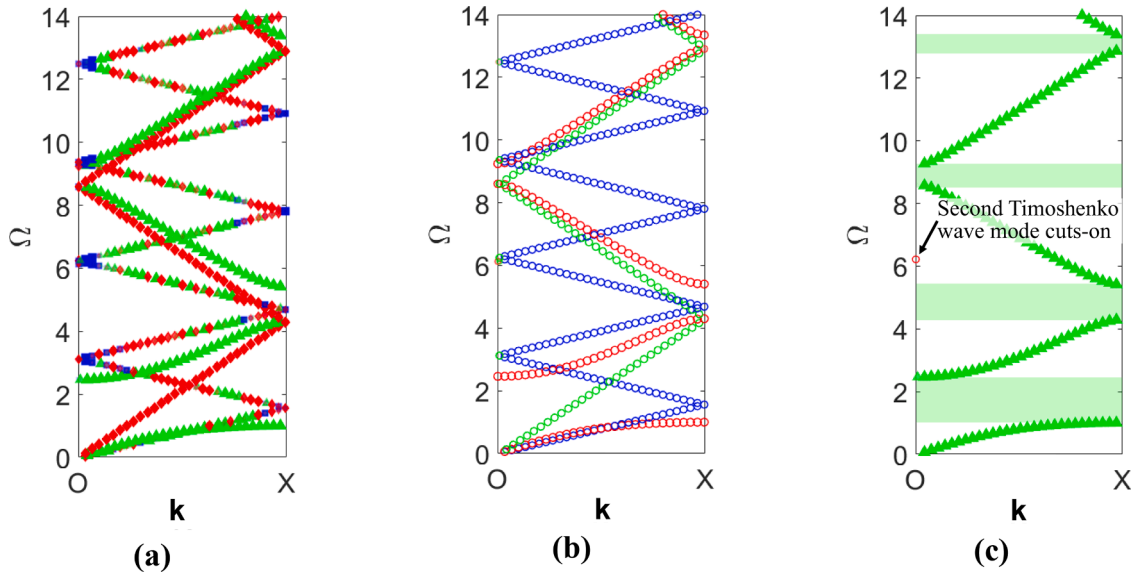


**Fig. 4.** Dispersion curves for the locally resonant sandwich beam, as studied in Ref. [6]. Fig. 4(a) shows the translational components and Fig. 4(b) shows the rotational components of the relative effective modal mass vectors. Fig. 4(c) shows only the flexural wave solution with translational motion along the 2-direction. The symbols and color scales are as shown in Fig. 2(c).

We then overlay these components on the dispersion points and account for each component's contribution using color intensity scales, where for each individual component, the lowest color intensity indicates a numerical value of 0, i.e., the component does not contribute to the motion, and the brightest color intensity indicates a numerical value of 1 and the component's dominance in the overall motion. For clearer visualization, we plot the translational and rotational relative effective modal mass vector components in two separate, adjacent plots. Similarly, to clearly distinguish the *S*- and *P*-waves, we separately plot the polarization factor at each eigenfrequency solution using the asterisk symbol with color intensity varying from cyan to black; cyan indicates a pure *S*-wave and black indicates a pure *P*-wave.

An example application of this visualization scheme is shown in Fig. 2. Here, we plot the dispersion curves of the square lattice previously shown in Fig. 1 using the visualization scheme explained above. As seen from the figures, the proposed visualization scheme makes it easier to accurately identify the wave propagation modes and clearly distinguish the polarization associated with each wave solution. In turn, this makes the identification of the various bandgaps more straightforward and accurate than visually analyzing the mode shapes at each point. For the remainder of the paper, we use this scheme when analyzing the wave propagation behavior of various structures.

#### 4. Method validation

In this section, we validate the presented method by comparing the propagation mode and polarization predictions to published results in the literature. First, we verify the method's efficacy in correctly predicting modal coupling by modeling the response of a beam that exhibits strong flexural-torsional coupling. Then, we use the method to identify the presence of local resonance and Bragg wave attenuation bandgaps in a locally resonant sandwich beam. Finally, we validate the presented methods ability to predict polarized bandgaps by modeling a 3D composite metastructure with periodically embedded inclusions that cause the emergence of longitudinal, flexural, and torsional bandgaps.

##### 4.1. Mode identification in a coupled beam

Consider a prismatic thin-walled cantilevered beam with an open, symmetric channel cross-section, as shown in Fig. 3. Originally studied by Noor et al. [71] using a mixed 1D FE approach and verified using a 2D

plate/shell model based on the Sanders-Budiansky shell theory, this beam exhibits strong flexural-torsional coupling that can be difficult to identify without visually analyzing the mode shapes. Here, to demonstrate the accuracy of the proposed method, we analyze the free vibration behavior of the beam and compare the mode types predicted using the relative effective modal mass vectors with those obtained by Noor et al. and by visually inspecting the individual mode shapes. We model the beam as a 3D deformable solid using continuum solid shell elements (CSS8), with its prismatic cross-section in the 2–3 plane and the length along the 1-axis; the geometrical and material parameters are chosen to match those used by Noor et al. and are summarized in Fig. 3.

We use a linear perturbation procedure to extract the first six eigenfrequencies and the corresponding eigenvectors, from which the corresponding relative effective modal mass vectors are calculated to help identify individual modes as flexural, torsional, or coupled (hybrid). The relative effective modal mass components and the mode shapes, as visualized in the solver (Abaqus CAE) are shown for each mode in Table 3.

In accordance with Noor et al. and the extracted mode shapes, the relative effective modal mass vectors predict strong flexural-torsional coupling in all the modes except the second and sixth modes—these are the first and second horizontal flexural modes, as evidenced by the pure translation along the 2-axis ( $q_{t_2}^n = 1$ ) and rotation about the 3-axis ( $q_{r_3}^n = 1$ ). The coupled behavior of the remaining four modes is evidenced by the vertical translation,  $q_{t_3}^n$ , occurring in combination with the flexure-associated rotation about the 2-axis,  $q_{r_2}^n$ , and the torsion-associated rotation about the 1-axis,  $q_{r_1}^n$ . Further, the degree of participation of the flexural and torsional motions in each coupled mode is seen by the relative values of the rotations associated with each motion: while the flexure-associated rotation dominates in modes one and five, the torsion-associated rotation dominates in modes three and four. This is also consistent with the strain energy based predictions obtained by Noor et al. Thus, the relative effective modal mass vector accurately identifies all six modes, including the coupled modes.

##### 4.2. Propagation mode and bandgap identification in a Timoshenko beam

Consider a sandwich beam with periodically embedded internal resonators, as studied previously by Sharma et al. [6]. The periodic insertion of spring-mass resonators results in the formation of flexural wave attenuation bandgaps due to local resonance and Bragg scattering effects.



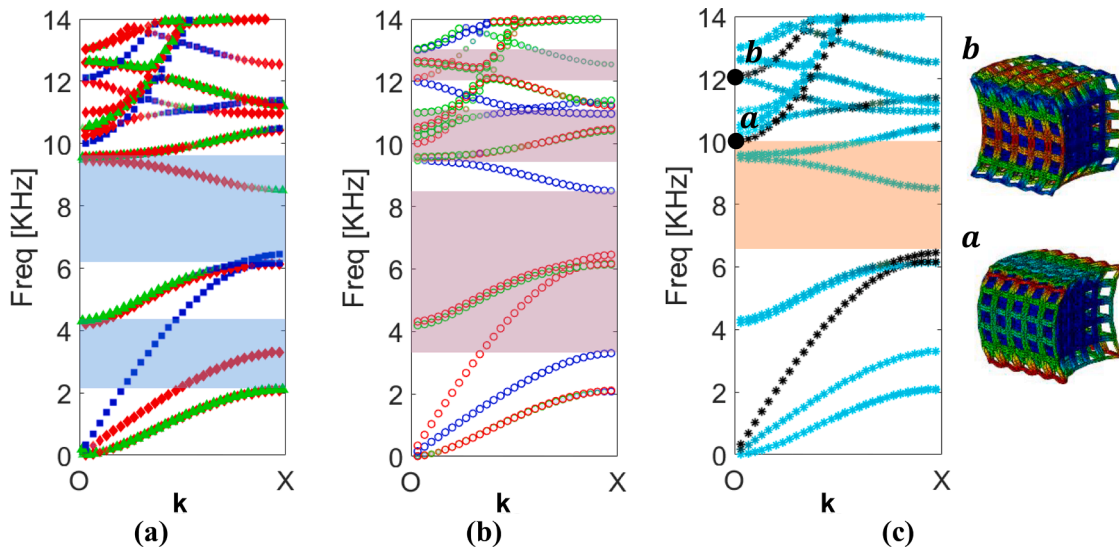


**Fig. 5.** Dispersion curves along the O-X wave vector direction for the composite 3D metastructure studied in Ref. [32]. Fig. 5(a) shows the translational components and Fig. 5(b) shows the rotational components of the relative effective modal mass vectors. Fig. 5(c) shows the polarization factors and the mode shapes at locations a and b. The shaded regions in Figs. 5(a), (b), and (c) are the identified flexural (blue), torsional (red), and longitudinal (orange) bandgaps.

Here, we model the sandwich beam as a Timoshenko beam using the material and geometrical parameters as described in Ref. [6] and obtain the dispersion curves using the previously described unit cell approach; the unit cell is chosen such that the resonator is connected to the central node and the Floquet-Bloch boundary conditions are applied at the end nodes. We model the beam as a 3D wire with its length along the  $I$ -axis, using shear-flexible beam elements with quadratic interpolation (B32). We extract the eigenvalues and eigenvectors using a linear perturbation procedure, carried out while sweeping the wave vector along the longitudinal ( $I$ -) direction. The extracted eigenvectors are then used to calculate the relative effective modal mass vectors using a Matlab script.

The dispersion curves with the identified propagation modes, allowing for motion along all degrees-of-freedom, are shown in Fig. 4(a-b), where all frequencies are normalized with respect to the local resonance frequency (200 Hz). For easier comparison with the published result in [6], Fig. 4(c) shows the dispersion curves obtained when only flexural displacements along the 2-axis and rotations about the 3-axis are permitted, in accordance with the assumptions made by Sharma et al. [6]. As expected, the dispersion curves for the sandwich beam with no restrictions on the degrees-of-freedom show multiple wave modes within the frequency range. The periodic insertion of local resonators causes a low-frequency bandgap around their resonance frequency, and multiple Bragg bandgaps at higher frequencies. Since the resonator motion is restricted to the 2-direction, all the generated bandgaps are polarized, only attenuating flexural waves with displacements polarized in the 2-direction. The presence of these polarized flexural bandgaps is seen more clearly in Fig. 4(c), where all the modes except the classical Timoshenko beam modes (flexural and a higher-order mode accounting for the shear deformation and rotational inertia) are suppressed. The predicted bandgaps match exactly the results shown in Fig. 3(b) in [6]. Additionally, the presence of the second Timoshenko mode is accurately captured at  $\Omega = 6.12$ , and clearly visualized by the hollow red circle, indicating the dominance of rotation about the 3-axis. Thus, the presented method, coupled with the visualization scheme, allows for an easy identification of each propagating wave mode and, consequently, the accurate assessment of the bandgap polarizations.

#### 4.3. Composite 3D-printed metastructure with embedded resonant inclusions

Finally, consider the wave attenuation behavior of the composite 3D-printed metastructure studied by Matlack et al. [32]. The metastructure

consists of steel inclusions coated with a thin layer of polycarbonate and periodically embedded within a 3D printed polycarbonate cubic lattice. This design results in the generation of low-frequency attenuation bandgaps driven by the interactions between the local resonance and Bragg bandgaps. Here, we replicate this design using the parameters provided in Ref. [32] and compare the predicted bandgaps with those obtained by Matlack et al. for the high-stiffness case shown in Fig. 2(a) in Ref. [32]. The metastructure is modeled as an infinite beam using three-dimensional, ten-node tetrahedral elements (C3D10). The dispersion curves along the O-X path are then overlaid by the relative modal effective mass vectors and shown in Fig. 5(a-c). For clarity, we plot the displacement components in Fig. 5(a), the rotations in Fig. 5(b), and the polarization factors in Fig. 5(c). We then mark the flexural bandgaps in Fig. 5(a), torsional bandgaps in Fig. 5(b), and longitudinal bandgaps in Fig. 5(c). The accuracy of the bandgap identification—performed without analyzing individual mode shapes for each  $\omega(\mathbf{k})$  point—is established by comparing the bandgap predictions in Ref. [32], Fig. S4.

In agreement with Ref. [32], the high-stiffness composite beam design results in distinct polarized bandgaps, which overlap to form a complete-directional bandgap ranging from 6400 Hz to 8400 Hz. While the predicted flexural bandgaps coincide with those identified in Ref. [32], some additional information is obtained using the relative modal effective mass vectors. First, we identify the presence of two additional torsional bandgaps—as evidenced by the dominant rotation about the axial direction—occurring at higher frequencies; these bandgaps would otherwise be difficult to identify using mode shape visualization. Secondly, the frequency range of the longitudinal bandgap, identified here using the polarization factors, is narrower than that identified in Ref. [32]. Using mode shape observation, the authors incorrectly identify the cut-on frequency of a higher-order longitudinal mode as the bandgap cut-off frequency. In actuality, the longitudinal mode cuts-on at a lower frequency, as correctly predicted by the polarization plot and verified by the mode shapes at locations  $a$  and  $b$ , as shown in Fig. 5(c). Thus, the presented method can help avoid the misidentification of propagation modes and bandgaps, especially due to the complex mode shapes occurring at higher frequencies.

## 5. Method application

In this section, we provide an example application of the developed method. We study the elastic wave propagation behavior of square planar lattices; specifically, we focus on the existence of polarized

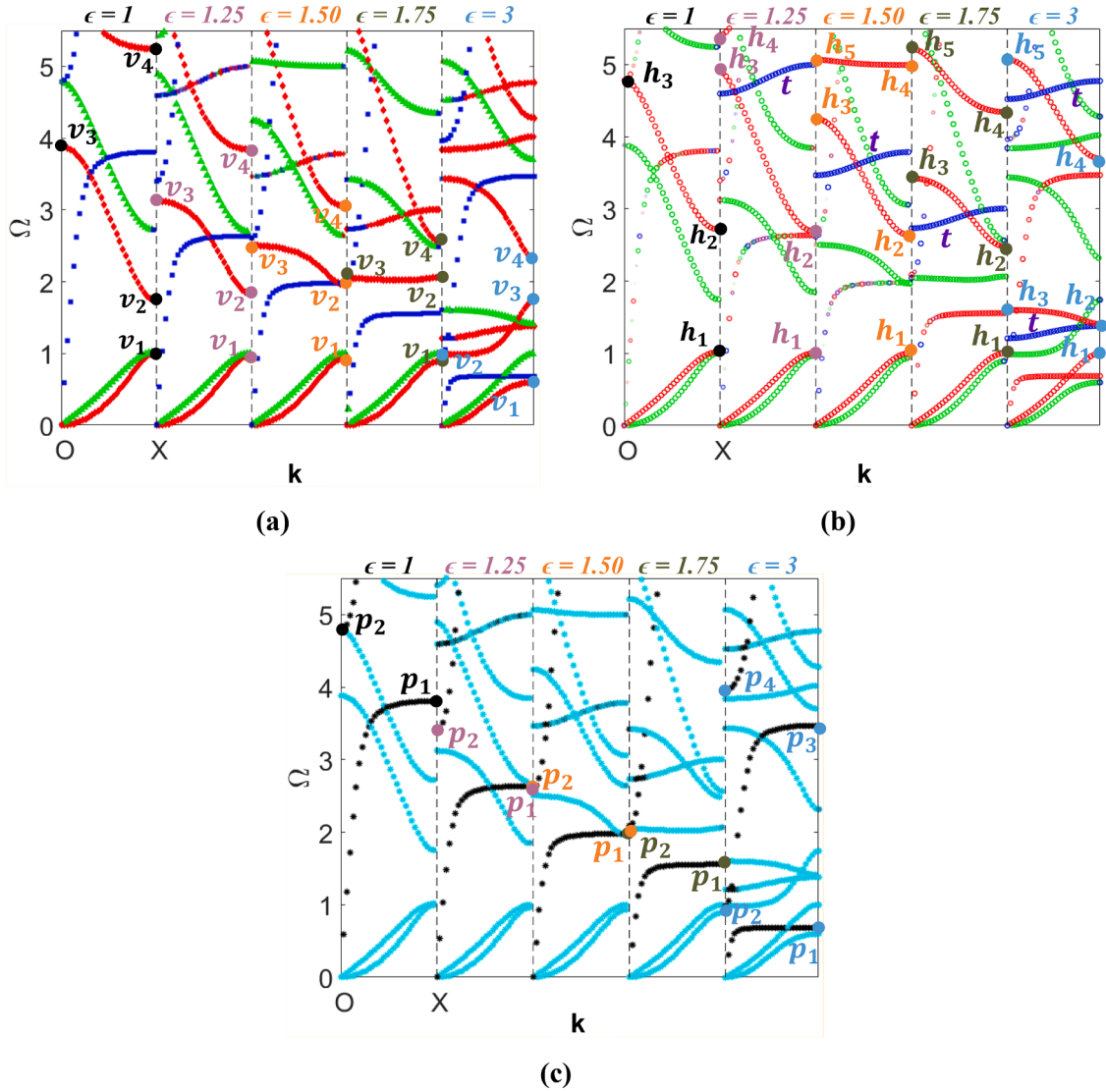


**Fig. 6.** Effect of variation of side length ratio,  $\epsilon$ , on the dispersion behavior and bandgap evolution along the O-X wave vector direction. The relative effective translational mass and cut-on and cut-off frequencies for SV-bandgaps ( $v_i$ ) are marked in Fig. 6(a); the relative effective rotational mass and cut-on and cut-off frequencies for SH-bandgaps ( $h_i$ ) are marked in Fig. 6(b); the polarization factors and the cut-on and cut-off frequencies for P-bandgaps ( $p_i$ ) are marked in Fig. 6(c). Curves marked as t in Fig. 6(b) indicate standing waves with motion dominated by rotations about the 1-axis.

bandgaps and the effect of lattice parameter perturbations on the individual bandgaps. We choose the square lattice previously studied in Section 2.1, and shown in Fig. 1, as the base lattice and systematically perturb its side length ratio ( $\epsilon$ ), internal angle skewness ( $\theta$ ), vertical strut cross-section ( $V$ ), and the joint connection type. We model all the lattices in Abaqus CAE using B32 beam elements with six degrees-of-freedom—i.e., out-of-plane modes are permitted—and the dispersion relations and mode identification information are extracted using the proposed method. For consistency of comparison, the mass of all lattices is maintained the same throughout. In the interest of clarity, we discuss the evolution of polarized bandgaps only along the O-X wave vector direction. Here, all eigenfrequencies are normalized with respect to the eigenfrequency of the first in-plane bending mode occurring at high-symmetry point X.

### 5.1. Effect of side length ratio

We define the side length ratio as  $\epsilon = L_2/L_1$ , where  $L_2$  and  $L_1$  are the unit cell lattice constants along the 2- and 1-axis, respectively. We modify the square lattice by incrementally increasing  $\epsilon$  while maintaining all the other lattice parameters, including its total mass, as

constants. The dispersion curves with the identified propagation modes and the associated polarization factors are plotted as a function of  $\epsilon$  along the O-X direction in Fig. 6. We plot the translational components in Fig. 6(a), rotational components in Fig. 6(b), and the polarization factors in Fig. 6(c). For clarity, the cut-on and cut-off frequencies for the SV-bandgaps are marked in Fig. 6(a) using symbols  $v_i$ , the SH-bandgaps are marked in Fig. 6(b) using symbols  $h_i$ , and the P-bandgaps are marked in Fig. 6(c) using symbols  $p_i$ . Here, we vary  $\epsilon$  from 1 (i.e., square lattice) to  $\epsilon = 1.75$ ; an extreme case of  $\epsilon = 3$  is also shown.

Within the considered frequency range, the dispersion curves for the square lattice,  $\epsilon = 1$ , show the presence of two SV-polarized bandgaps ( $v_1$ -to- $v_2$  and  $v_3$ -to- $v_4$ ), two SH-polarized bandgap ( $h_1$ -to- $h_2$  and  $h_3$  and beyond), and one P-polarized bandgap ( $p_1$ -to- $p_2$ ) along the O-X direction. The SV- and SH-bandgaps overlap between  $\Omega = 1$  to 1.748, indicating that only P-waves can propagate through the lattice along O-X within this frequency range. This behavior is akin to the “fluid-like” behavior recently demonstrated by Ma et al. [33] for a three-dimensional elastic metamaterial with an anisotropic locally resonant unit cell. As the side length ratio is increased, the reduction in lattice symmetry lifts the degeneracy between the SV- and SH-eigenmodes occurring at the high-symmetry point X at  $\Omega = 1$  for the square

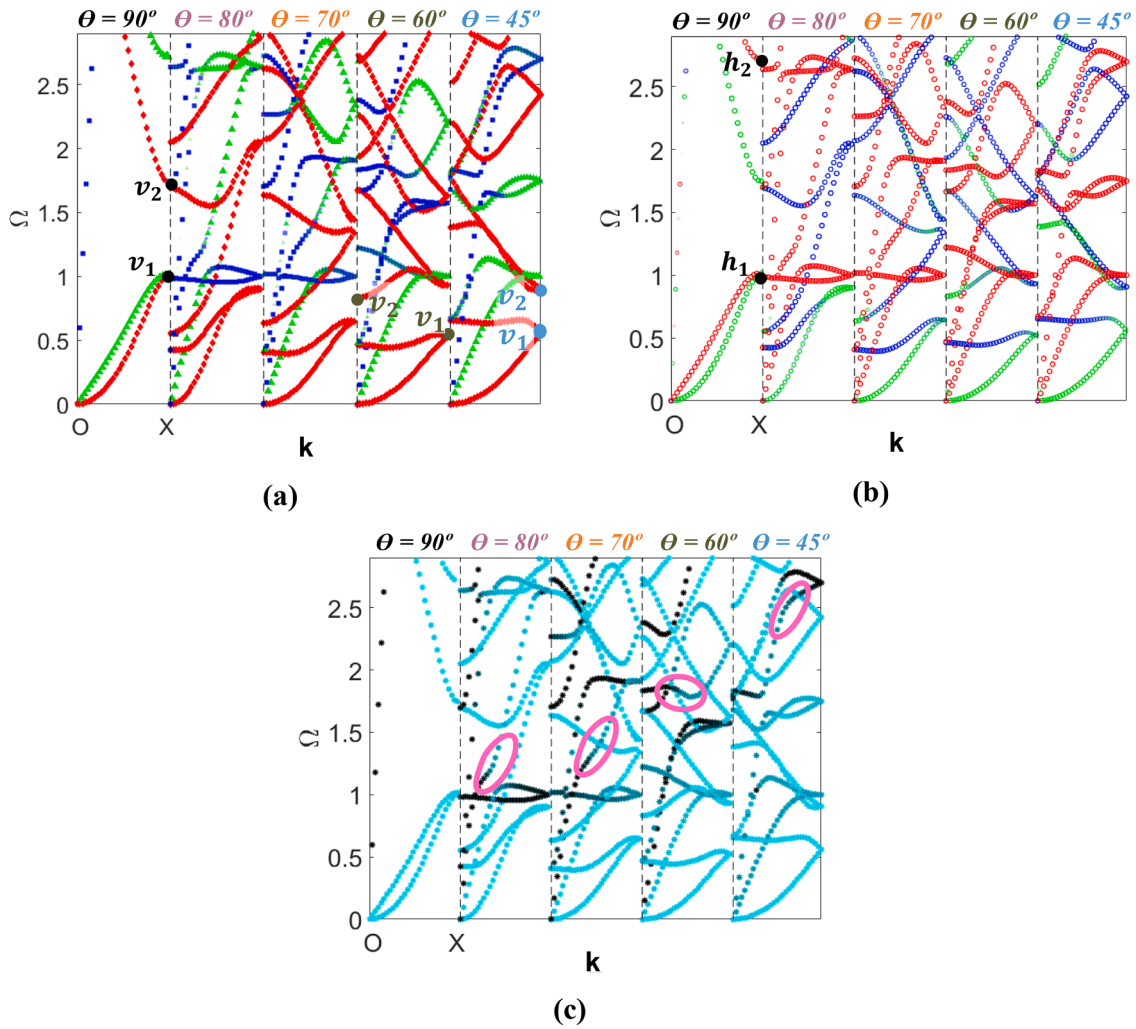


**Fig. 7.** Effect of variation of lattice internal angle,  $\theta$ , on the dispersion behavior and bandgap evolution along the O-X wave vector direction. The relative effective translational mass and cut-on and cut-off frequencies for SV-bandgaps ( $v_i$ ) are shown in Fig. 7(a); the relative effective rotational mass and cut-on and cut-off frequencies for SH-bandgaps ( $h_i$ ) are shown in Fig. 7(b); the polarization factors are shown in Fig. 7(c), where the elliptical markings show examples of mode conversion between P- and S-wave propagation modes.

lattice. As  $\varepsilon$  increases, the lower bound of the first SV-bandgap,  $v_1$ , gradually shifts to a lower frequency while the upper bound,  $v_2$ , shifts to a higher frequency, causing an increase in the first SV-bandgap width with increasing  $\varepsilon$ . On the other hand, while the lower bound of the first SH-bandgap,  $h_1$ , remains stationary because it is the normalization frequency, the upper bound,  $h_2$ , gradually shifts to a lower frequency and results in a reduction in the first SH-bandgap width with increasing  $\varepsilon$ . While these changes in the first SH- and SV-bandgap widths may be considered insignificant, the changes observed in the higher order bandgaps are more pronounced. Increasing  $\varepsilon$  reduces the width of the second SV-bandgap while shifting it to a comparatively lower frequency range. Similarly, the second SH-bandgap shifts to lower frequencies with increasing  $\varepsilon$ ; however, in contrast with the second SV-bandgap, the width of this bandgap increases with increasing  $\varepsilon$  and an ultrawide SH-bandgap emerges for the extreme case of  $\varepsilon = 3$ . Further, the comparative beginning and end locations of the bandgap bounding curves indicate that for both SH- and SV-polarizations, the first bandgaps are driven by Bragg effects while the second bandgaps occur due to lattice resonance effects [6]. These observations align with the fact that increasing  $\varepsilon$  does not alter the lattice periodicity along O-X, but it reduces the effective lattice stiffness along the 2- and 3-axis, thus reducing the lattice structural resonance frequencies responsible for the second bandgaps. For the extreme case of  $\varepsilon = 3$ , the first SV-bandgap changes into a resonance-driven gap while the second SV-bandgap changes into a

Bragg bandgap. Interestingly, a nearly flat band, marked as  $t$  in Fig. 6(b), with dominant rotations about the 1-axis appears at  $\varepsilon = 1.25$  and shifts to lower frequencies with increasing  $\varepsilon$ ; two such bands are observed for  $\varepsilon = 3$ . The flatness of these bands indicate that these are rotational standing waves resembling torsional behavior in finite structures.

The effect of this stiffness reduction is also observed on the P-bandgap, which is generated due to the first structural resonance occurring in the vertical lattice struts oriented perpendicular to the wave propagation direction, as evidenced by the behavior of the upper and lower bounding curves. As  $\varepsilon$  increases, the reduction in the effective stiffness reduces the resonance frequency,  $p_1$ , and shifts the P-bandgap to a lower frequency. Eventually, for the case of  $\varepsilon = 1.75$ , the P-bandgap overlaps with the first SV- and SH-bandgaps between  $\Omega = 1.75$  to 2.5, resulting in the emergence of a complete-directional bandgap where all waves along O-X are spatially attenuated, irrespective of their polarizations. For the extreme case of  $\varepsilon = 3$ , the interactions between the individual resonance and Bragg effects result in the uncoupling of the first SV- and SH-bandgaps, but an overlap of the P- and SV-bandgaps results in the emergence of a frequency region where only waves with SH-polarization can propagate through the lattice.

## 5.2. Effect of lattice internal angle

The variation in the dispersion curves and the wave polarizations

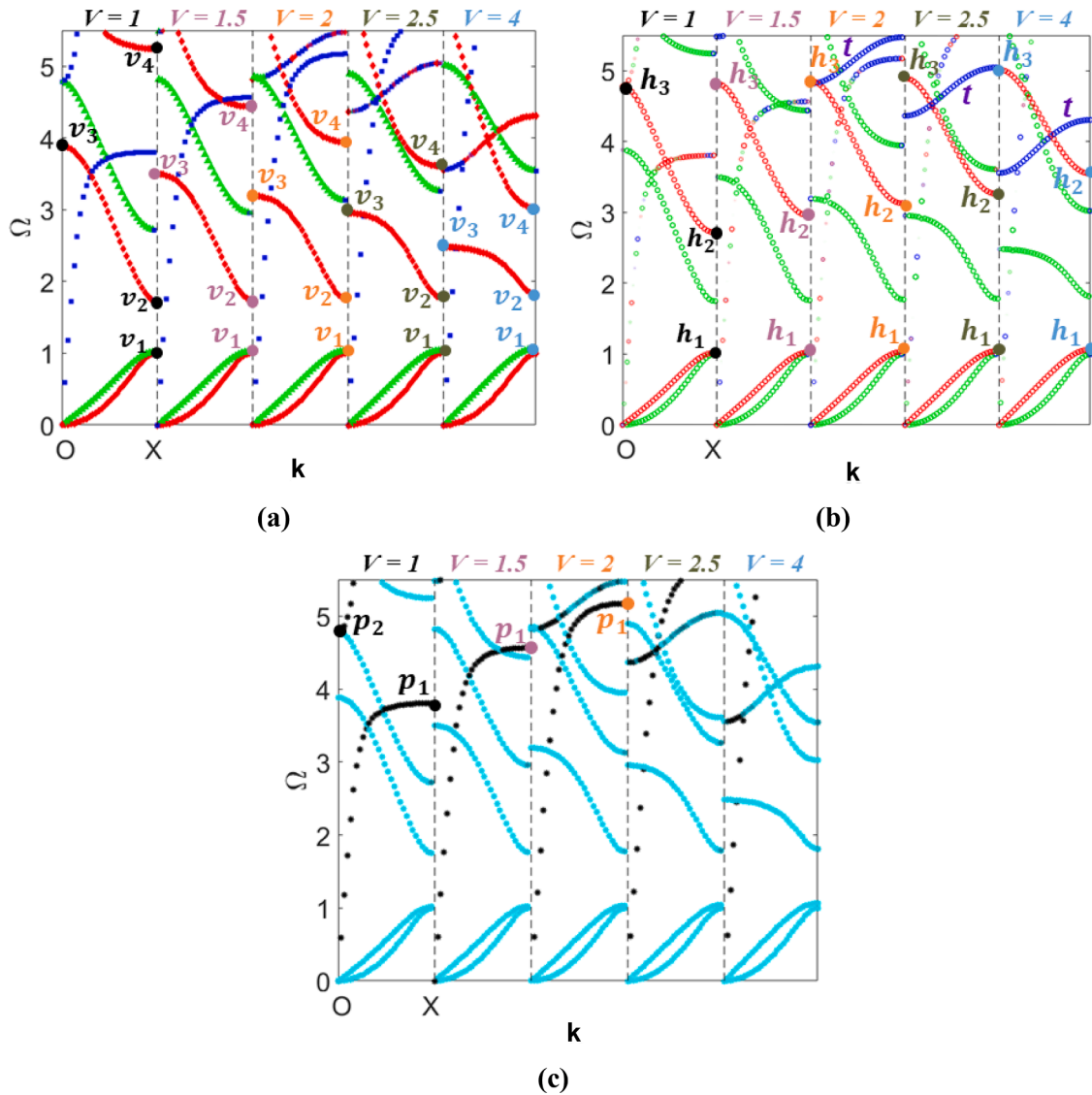


**Fig. 8.** Effect of variation of vertical strut cross-sectional width ratio,  $V$ , on the dispersion behavior and bandgap evolution along the O-X wave vector direction. The relative effective translational mass and cut-on and cut-off frequencies for SV-bandgaps ( $v_i$ ) are shown in Fig. 8(a); the relative effective rotational mass and cut-on and cut-off frequencies for SH-bandgaps ( $h_i$ ) are shown in Fig. 8(b); the polarization factors and the cut-on and cut-off frequencies for P-bandgaps ( $p_i$ ) are marked in Fig. 8(c). Curves marked as  $t$  in Fig. 8(b) indicate standing waves with motion dominated by rotations about the 1-axis.

along the O-X direction as a function of the lattice internal angle,  $\theta$ , are shown in Fig. 7. Here, we vary  $\theta$  by changing the orientation of the vertical strut with respect to the horizontal lattice strut. In contrast to the variation in  $\varepsilon$ , a change in  $\theta$  drastically changes the dispersion behavior of the lattice, indicating that the elastic wave propagation behavior of the lattice is significantly more sensitive to rotational symmetries in the lattice. Given the high number of low frequency modes for the skewed lattices, we restrict the analysis in this case to  $\Omega = 2.5$ .

Altering the square lattice ( $\theta = 90^\circ$ ) to a skewed lattice with  $\theta = 80^\circ$  results in the disappearance of the previously observed Bragg SV- and SH-bandgaps originating at  $\Omega = 1$ , marked as  $v_1$ -to- $v_2$  and  $h_1$ -to- $h_2$ , respectively. Instead, the angular distortion results in the appearance of multiple new SV-propagation modes, different from those observed within the same frequency range for the square lattice—the new modes are dominated by out-of-plane motion coupled with torsion-like rotations about the 1-axis. As the angular distortion is increased, a low-frequency SV-bandgap reappears for the cases of  $\theta = 60^\circ$  and  $45^\circ$ . Altering the orientation of the vertical struts also introduces additional stiffness in the horizontal direction, as evidenced by the increase in the slope of the first SH-curve. Further, the relative orientation of the lattice

struts with respect to the wave vector orientation causes in-plane coupling and mode transitions in the P- and SH-modes. These coupled in-plane propagation modes are more clearly observed in the polarization angle plots, Fig. 7(c), where the darker dispersion points indicate a higher contribution of lattice motion parallel to the wave vector direction—representative cases of transitions between the two modes within the same propagation band are marked in Fig. 7(c). Thus, the polarization plots allow an easier identification of the P-wave solutions and the corresponding identification of frequency regions where such waves cannot propagate.

### 5.3. Effect of vertical strut cross-section width

In this case, we modify the lattice by changing the cross-sectional shape of the vertical strut; the vertical strut is altered by changing the ratio of the cross-sectional widths along the 1- and the 3-directions. Assuming the cross-sectional width ratio equal to 1 as the base lattice configuration—i.e., a square lattice made using square horizontal and vertical struts—we alter the vertical strut shape by increasing its cross-sectional width ratio while maintaining its cross-sectional area, and

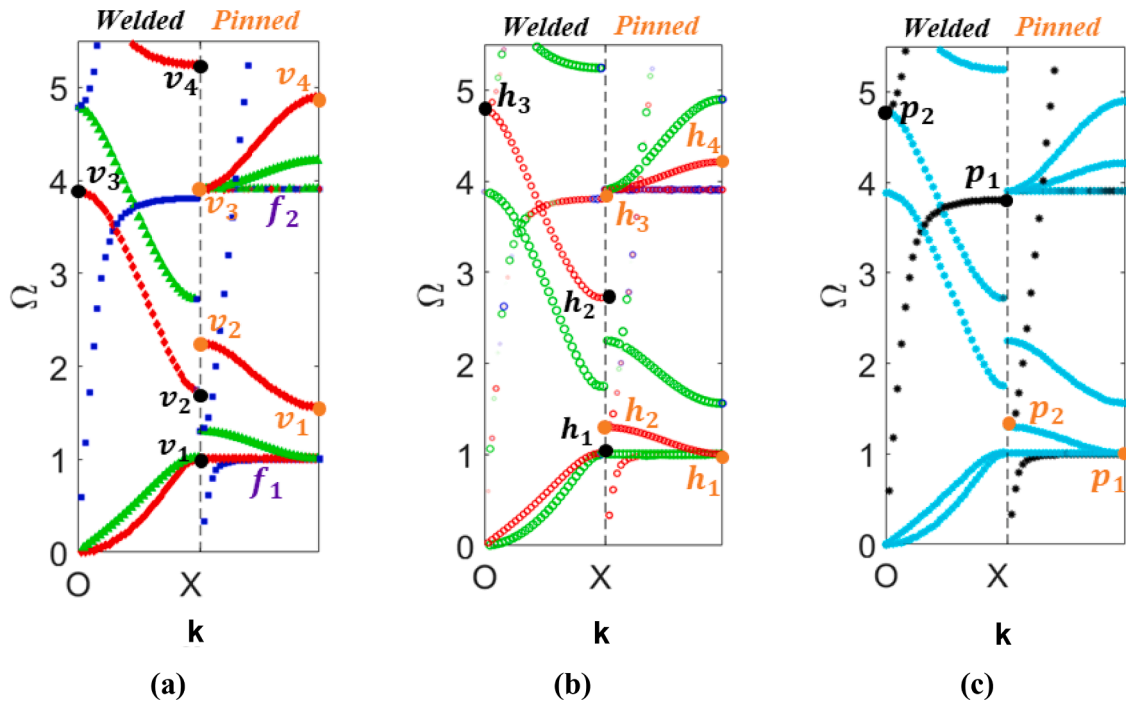


**Fig. 9.** Effect of changing lattice joint type from welded to pinned on the dispersion behavior and bandgap evolution along the O-X wave vector direction. The relative effective translational mass and cut-on and cut-off frequencies for SV-bandgaps ( $v_i$ ) are shown in Fig. 9(a); the relative effective rotational mass and cut-on and cut-off frequencies for SH-bandgaps ( $h_i$ ) are shown in Fig. 9(b); the polarization factors and the cut-on and cut-off frequencies for P-bandgaps ( $p_i$ ) are marked in Fig. 9(c). Curves marked as  $f_1$  and  $f_2$  in Fig. 9(a) indicate standing waves or structural resonances in the pinned joint lattice.

consequently the overall lattice mass, as a constant. We use the symbol  $V$  to denote the rectangularity of the vertical strut. All the other lattice parameters, including the lattice constants  $L_1$  and  $L_2$  are kept constant.

The dispersion curves and the wave polarizations along the O-X direction as a function of  $V$ , are shown in Fig. 8. Overall, the first SV-bandgap remains unaffected by the changes in  $V$  since this bandgap is generated due to the Bragg effects and is bounded by the out-of-plane motion of the horizontal struts. While the lower bounding frequency of the first SH-bandgap ( $h_1$ ) is similarly unaffected by changes in  $V$ , the upper bounding frequency ( $h_2$ ) increases with increasing  $V$ , resulting in widening this bandgap.

By contrast, the second SV-bandgap ( $v_3$ -to- $v_4$ ), generated by structural resonance effects, shifts to a lower frequency with increasing  $V$  because of the accompanying reduction in the out-of-plane stiffness of the vertical struts. This gap eventually overlaps with the first SH-bandgap and forms a directional S-bandgap where only P-waves can propagate ( $V = 2.5$ ). Note that a similar bandgap was observed when increasing  $\epsilon$  in section 5.1; however, in that case, the overlapping SV- and SH-bandgaps are both generated by Bragg effects.

Further, increasing  $V$  increases the vertical strut’s in-plane stiffness and causes the first P-bandgap ( $p_1$ -to- $p_2$ )—driven by vertical strut resonances—to shift to higher frequencies. A propagation mode dominated by rotations about the  $I$ -axis, marked as  $t$  in Fig. 8(b) and similar to that observed in Section 5.1, is seen around  $\Omega = 5$  for  $V = 2$ . This rotational mode with significant coupling between the P- and SV-modes, likely results from the vertical strut cross-sectional asymmetry and shifts to lower frequencies with increasing  $V$ , eventually converting into a propagation mode that transitions from a pure P-mode to a pure SV-mode for the extreme case of  $V = 4$ .

#### 5.4. Effect of change in lattice joint

Here, we consider the effect of changing the nature of the joint connecting the horizontal and vertical struts of a square lattice. Previously, Wang et al. [30] have considered the effect of joint connectivity

on the wave propagation behavior of triangular and hexagonal Euler-Bernoulli lattice structures. Their results demonstrate that altering the connectivity induces local resonance effects which may or may not result in the generation of complete bandgaps, depending on the global lattice topology.

The dispersion curves and wave polarization plots of the square lattices with welded and pinned joints are compared in Fig. 9. In line with the observations by Wang et al. [30], altering the joint connectivity of the square lattice to a pinned joint significantly changes its dispersion behavior; specifically, two flat dispersion curves (marked as  $f_1$  and  $f_2$ )—indicating standing waves or structural resonances—absent in the welded lattice are observed for the pinned lattice. Interestingly, the pinned lattice shows multiple, wide S-bandgaps, including ultralow-frequency SH- and SV-bandgaps that extend to 0 Hz—indicating a propagation cut-on frequency below which all S-waves are spatially attenuated. The cut-on frequency for SH-waves ( $h_1$ ) is lower than that for the SV-waves ( $v_1$ ), i.e., the pinned lattice predominantly behaves as a fluid-like medium, by only supporting the propagation of P-waves below the first lattice element flexural resonance frequency. A P-bandgap ( $p_1$ -to- $p_2$ ) is also observed above this resonance frequency, which overlaps with the SV-bandgap and results in a frequency zone where only SH-waves can propagate through the structure. The second SH- and SV-bandgaps are caused due to Bragg effects, and both terminate at the second structural resonance ( $v_3$  and  $h_3$  are located on the flat band  $f_2$ ). The overlap between these bandgaps generates a second fluid-like behavior frequency region extending between  $v_2$  and  $v_3$ . It should be noted that the presence of an ultralow S- bandgap can also be seen in the results by Wang et al. (see Fig. S8(d) in Supplementary Information accompanying [30]); the presented visualization scheme makes it easier to identify this and other emergent behaviors, such as fluid-like behavior of square lattices with pinned joints, which may otherwise be easily missed.

#### 6. Conclusion

In this paper, we presented a new method for accurately identifying

the propagation mode and polarization of elastic waves traveling in periodic structures and architected metamaterials. Proposed as an alternative to the commonly used visual mode inspection technique, our method adapts the concept of the modal participation factor to quantify the relative participation of each directional motion component to the overall mode shape associated with a given eigenfrequency. This information is used to calculate the normalized relative effective translational and rotational mass components of the structure at each propagation mode, which are then used to identify the wave propagation mode associated with each dispersion solution. While this information is sufficient for identifying the associated polarization of low-frequency elastic waves in structures oriented along the wave vector, we propose the use of a new polarization factor to avoid misidentification of polarizations for more complex cases. Further, we propose a new visualization scheme where the relative effective mass and polarization factors are superposed over the conventional dispersion curve to quickly identify the presence of directional and polarized wave attenuation bandgaps.

The robustness of the proposed method was demonstrated by comparing our predictions against previously published results. First, we validated the method’s ability to identify mode shapes by simulating the free vibration behavior of a beam with an open, symmetric channel cross-section which exhibits strong flexural-torsional coupling. Our results show that the method accurately identifies the pure as well as the coupled mode shapes and is consistent with visual and strain energy based predictions. Next, we validated the method’s ability to identify wave propagation modes and the presence of attenuation bandgaps by modeling a locally resonant sandwich beam with periodically embedded internal resonators. The method accurately predicts the existence of bandgaps generated by local resonance and Bragg effects and shows that the generated bandgaps only attenuate flexural waves polarized along the active spring direction while allowing all other waves to propagate through the structure. Finally, we demonstrated the effectiveness of the method and the proposed visualization scheme by investigating the directional-polarized bandgaps of a composite 3D printed metastructure with embedded resonant inclusions. Specifically, we showed that the relative effective mass and polarization factor accurately predict the polarizations of the propagation solutions and that the visualization scheme makes it easier to correctly identify the emergent bandgaps, especially those associated with the complicated mode shapes occurring at higher frequencies.

Finally, to demonstrate the effectiveness of the developed method, we used it to study the effect of lattice and structural parameter perturbations on the wave propagation behavior of a planar square beam lattice. Despite being widely studied, our analysis using the presented method reveals previously unobserved emergent behaviors and dispersion properties. Our analysis shows that breaking the underlying geometrical symmetry of the square lattice causes the emergence of

various polarized bandgaps, whose frequency range depends on the specific geometrical parameter being altered. The overlap between the *SH*- and *SV*- bandgaps results in the formation of a frequency region within which the solid lattice demonstrates a “fluid-like” behavior wherein only *P*-waves propagate through the structure. Overall, the dispersion behavior of the square lattice is significantly more sensitive to changes in the internal lattice angle and any alterations in the relative orientation of the lattice struts causes in-plane coupling and mode transitions in the *P*- and *SH*- modes. Furthermore, altering the connectivity of the vertical and horizontal struts from a welded joint to a pinned joint results in the emergence of ultralow-frequency *SH*- and *SV*-bandgaps that extend to 0 Hz, indicating that the pinned square lattice predominantly behaves as a fluid-like medium at frequencies below the first flexural resonance frequency of the pinned lattice struts.

Thus, the presented method provides a robust computational approach for studying the elastic wave propagation behavior of periodic media such as phononic structures, architected materials, layered composites, and metamaterials without resorting to the visual inspection of individual mode shapes.

**CRedit authorship contribution statement**

**Maria Carrillo-Munoz:** Conceptualization, Methodology, Software, Validation, Investigation, Writing – original draft, Visualization. **Bhisham Sharma:** Conceptualization, Methodology, Formal analysis, Resources, Project administration, Writing – review & editing, Supervision.

**Declaration of Competing Interest**

The authors declare that they have no known competing financial interests or personal relationships that could have appeared to influence the work reported in this paper.

**Data availability**

Data will be made available on request.

**Acknowledgment**

This research did not receive any specific grant from funding agencies in the public, commercial, or not-for-profit sectors.

**Appendix**

[Table A1](#), [Table A2](#)

**Table A1**

The calculated modal effective mass vectors, relative effective modal mass vectors, and the identified propagation mode for the locations marked in Fig. 1.

Location	Normalized frequency $\Omega^n$	Modal effective mass vectors $m_{eff}^n$	Relative effective translational mass $q_t^n = \langle q_{t_1}^n, q_{t_2}^n, q_{t_3}^n \rangle$	Relative effective rotational mass $q_r^n = \langle q_{r_1}^n, q_{r_2}^n, q_{r_3}^n \rangle$	Propagation mode
<i>a</i>	0.978	(0, 0, 20.931, 0, 0.010, 0)	(0, 0, 1)	(0, 1, 0)	Out-of-plane
<i>b</i>	1.000	(0.0, 21.202, 0, 0, 0, 0.002)	(0, 1, 0)	(0, 0, 1)	In-plane
<i>c</i>	1.738	(0, 0, 0.146, 0, 0.985, 0)	(0, 0, 1)	(0, 1, 0)	Out-of-plane
<i>c</i> <sub>1</sub>	3.412	(14.390, 0, 0, 0, 0, 0)	(1, 0, 0)	(0.003, 0.996, 0)	In-plane
<i>c</i> <sub>2</sub>	3.402	(0, 0, 0.183, 0, 0.292, 0)	(0, 0, 1)	(0, 1, 0)	Out-of-plane
<i>d</i> <sub>1</sub>	3.481	(0, 0, 0.125, 0, 0.246, 0)	(0, 0, 1)	(0, 1, 0)	Out-of-plane
<i>d</i> <sub>2</sub>	3.493	(13.239, 0, 0, 0, 0, 0)	(1, 0, 0)	(0, 0.994, 0.006)	In-plane
<i>e</i> <sub>1</sub>	10.079	(0, 0.02, 0, 0, 0, 0)	(0, 1, 0)	(0, 0, 1)	In-plane
<i>e</i> <sub>2</sub>	10.985	(0, 1.233, 0, 0, 0, 0)	(0, 1, 0)	(0, 0, 1)	In-plane
<i>f</i> <sub>1</sub>	2.692	(0, 0.013, 0, 0, 0, 1.260)	(0, 1, 0)	(0, 0, 1)	In-plane
<i>f</i> <sub>2</sub>	1.866	(14.4, 0, 0, 0, 0, 0)	(1, 0, 0)	(0, 0, 1)	In-plane
<i>g</i>	2.985	(7.21, 7.21, 0, 0, 0, 0.297)	(0.5, 0.5, 0)	(0, 0, 1)	In-plane
<i>h</i>	3.193	(8.309, 8.309, 0, 0, 0, 0)	(0.5, 0.5, 0)	(0.195, 0.038, 0.767)	In-plane

Table A2

The calculated translational modal participation factor, local wave vector orientation, polarization factor, and the identified wave polarization for the locations marked in Fig. 1.

Location	Normalized frequency $\Omega^n$	Translational components of the modal participation factor $\Gamma_t^n$	Local wave vector $k_d$	Polarization factor $\Phi^n$	Wave polarization
<i>a</i>	0.978	(0, 0, 0.691)	(1, 0, 0)	0	SV-wave
<i>b</i>	1.00	(0, 0.976, 0)	(1, 0, 0)	0	SH-wave
<i>c</i>	1.738	(0, 0, 0.143)	(1, 0, 0)	0	SV-wave
<i>c<sub>1</sub></i>	3.412	(1.827, 0, 0)	(1, 0, 0)	1	P-wave
<i>c<sub>2</sub></i>	3.402	(0, 0, -0.116)	(1, 0, 0)	0	SV-wave
<i>d<sub>1</sub></i>	3.481	(0, 0, -0.150)	(1, 0, 0)	0	SV-wave
<i>d<sub>2</sub></i>	3.493	(1.346, 0, 0)	(1, 0, 0)	1	P-wave
<i>e<sub>1</sub></i>	10.079	(0, -0.013, 0)	(1, 0, 0)	0	SH-wave
<i>e<sub>2</sub></i>	10.985	(0, 0.493, 0)	(1, 0, 0)	0	SH-wave
<i>f<sub>1</sub></i>	2.692	(0, 0.007, 0)	(1, 0, 0)	0	SH-wave
<i>f<sub>2</sub></i>	1.866	(0.156, 0, 0)	(0, 1, 0)	0	SH-wave
<i>g</i>	2.985	(0.497, -0.497, 0)	(-1, -1, 0)	0	SH-wave
<i>h</i>	3.193	(0.566, 0.566, 0)	(-1, -1, 0)	1	P-wave

## References

- Hussein MI, Leamy MJ, Ruzzene M. Dynamics of Phononic Materials and Structures: historical origins, recent progress, and future outlook. *Appl Mech Rev* 2014;66.
- Cummer SA, Christensen J, Alù A. Controlling sound with acoustic metamaterials. *Nat Rev Mater* 2016;1:1–13.
- Ma G, Sheng P. Acoustic metamaterials: from local resonances to broad horizons. *Sci Adv* 2016;2:e1501595.
- Cui TJ, Smith DR, Liu R. *Metamaterials*. Springer; 2010.
- Liu L, Hussein MI. Wave motion in periodic flexural beams and characterization of the transition between Bragg scattering and local resonance. *J Appl Mech* 2012;79.
- Sharma B, Sun CT. Local resonance and Bragg bandgaps in sandwich beams containing periodically inserted resonators. *J Sound Vib* 2016;364:133–46.
- Raghavan L, Phani AS. Local resonance bandgaps in periodic media: theory and experiment. *J Acoust Soc Am* 2013;134:1950–9.
- Cenedese M, Belloni E, Braghin F. Interaction of Bragg scattering bandgaps and local resonators in mono-coupled periodic structures. *J Appl Phys* 2021;129:124501.
- Crampin S. A review of wave motion in anisotropic and cracked elastic-media. *Wave Motion* 1981;3:343–91.
- Crampin S. An introduction to wave propagation in anisotropic media. *Geophys J Int* 1984;76:17–28.
- Armstrong G. Coupling between torsional and bending modes of vibration in cantilever beams. Durham University; 1972.
- Mace BR, Manconi E. Wave motion and dispersion phenomena: veering, locking and strong coupling effects. *J Acoust Soc Am* 2012;131:1015–28.
- Manconi E, Mace B. Veering and strong coupling effects in structural dynamics. *J Vib Acoust* 2017;139:021009.
- Jo SH, Shin YC, Choi W, Yoon H, Youn BD, Kim M. Double defects-induced elastic wave coupling and energy localization in a phononic crystal. *Nano Converg* 2021; 8:27.
- Mizuino S. Resonance and mode conversion of phonons scattered by superlattices with inhomogeneity. *Phys Rev B* 2003;68:193305.
- Joel N. Reflection and polarization of elastic waves in a lif crystal: mode conversion from longitudinal to transverse. *Proc Phys Soc* 1961;78:38 (1958-1967).
- Boudouti EHE, Djafari-Rouhani B, Akjouj A, Dobrzynski L. Acoustic waves in solid and fluid layered materials. *Surf Sci Rep* 2009;64:471–594.
- De Ponti JM, Iorio L, Riva E, Arditto R, Braghin F, Corigliano A. Selective mode conversion and rainbow trapping via graded elastic waveguides. *Phys Rev Appl* 2021;16:034028.
- Kato H, Maris HJ, Tamura SI. Resonant-mode conversion and transmission of phonons in superlattices. *Phys Rev B* 1996;53:7884.
- Lee J, Park J, Park CW, Cho SH, Kim YY. Uni-modal retroreflection in multi-modal elastic wave fields. *Int J Mech Sci* 2022;232:107655.
- Willis J. Polarization approach to the scattering of elastic waves—I. Scattering by a single inclusion. *J Mech Phys Solids* 1980;28:287–305.
- Manzanares-Martinez B, Ramos-Mendieta F. Sagittal acoustic waves in phononic crystals: k-dependent polarization. *Phys Rev B* 2007;76:134303.
- Kraut EA. Advances in the theory of anisotropic elastic wave propagation. *Rev Geophys* 1963;1:401–48.
- Anderson DL. Elastic wave propagation in layered anisotropic media. *J Geophys Res* 1961;66:2953–63.
- Musgrave M. The propagation of elastic waves in crystals and other anisotropic media. *Rep Prog Phys* 1959;22:74.
- Bacigalupo A, Lepidi M. Acoustic wave polarization and energy flow in periodic beam lattice materials. *Int J Solids Struct* 2018;147:183–203.
- Machado M, Moura B, Dey S, Mukhopadhyay T. Bandgap manipulation of single and multi-frequency smart metastructures with random impedance disorder. *Smart Mater Struct* 2022;31:105020.
- Meaud J, Che K. Tuning elastic wave propagation in multistable architected materials. *Int J Solids Struct* 2017;122:69–80.
- Celli P, Gonella S. Low-frequency spatial wave manipulation via phononic crystals with relaxed cell symmetry. *J Appl Phys* 2014;115:103502.
- Wang P, Casadei F, Kang SH, Bertoldi K. Locally resonant band gaps in periodic beam lattices by tuning connectivity. *Phys Rev B* 2015;91.
- Bergamini A, Delpero T, Simoni LD, Lillo LD, Ruzzene M, Ermanni P. Phononic crystal with adaptive connectivity. *Adv Mater* 2014;26:1343–7.
- Matlack KH, Bauhofer A, Krodel S, Palermo A, Daraio C. Composite 3D-printed metastructures for low-frequency and broadband vibration absorption. *Proc Natl Acad Sci U S A*, 2016;113:8386–90.
- Ma G, Fu C, Wang G, Del Hougne P, Christensen J, Lai Y, Sheng P. Polarization bandgaps and fluid-like elasticity in fully solid elastic metamaterials. *Nat Commun* 2016;7:1–8.
- Bayat A, Gaitanaros S. Wave Directionality in Three-Dimensional Periodic Lattices. *J Appl Mech* 2017:85.
- Ruzzene M, Scarpa F, Soranna F. Wave beaming effects in two-dimensional cellular structures. *Smart Mater Struct* 2003;12:363–72.
- Zelhofer AJ, Kochmann DM. On acoustic wave beaming in two-dimensional structural lattices. *Int J Solids Struct* 2017;115-116:248–69.
- Manzanares-Martínez B, Sánchez-Dehesa J, Håkansson A, Cervera F, Ramos-Mendieta F. Experimental evidence of omnidirectional elastic bandgap in finite one-dimensional phononic systems. *Appl Phys Lett* 2004;85:154–6.
- De Ponti JM, Riva E, Braghin F, Arditto R. Elastic three-dimensional metaframe for selective wave filtering and polarization control. *Appl Phys Lett* 2021;119:211903.
- Colombi A, Craster RV, Colquitt D, Achaoui Y, Guenneau S, Roux P, Rupin M. Elastic wave control beyond band-gaps: shaping the flow of waves in plates and half-spaces with subwavelength resonant rods. *Front Mech Eng* 2017;3:10.
- Wang Y, Li Z, Golub MV, Huang G, Chen W, Zhang C. Interfacial delamination-induced unidirectional propagation of guided waves in multilayered media. *Math Mech Solids* 2022;10812865221092680.
- Miao H, Li F. Shear horizontal wave transducers for structural health monitoring and nondestructive testing: a review. *Ultrasonics* 2021;114:106355.
- Helbig K, Carcione JM. Anomalous polarization in anisotropic media. *Eur J Mech A Solids* 2009;28:704–11.
- Lee HJ, Lee JR, Moon SH, Jeon EC, Kim K, Kim YY. Off-centered double-slit metamaterial for elastic wave polarization anomaly. *Sci Rep* 2017;7:15378.
- Patil GU, Matlack KH. 3D auxetic lattice materials for anomalous elastic wave polarization. *J Acoust Soc Am* 2019;145:1259.
- Huang H, Sun C. Wave attenuation mechanism in an acoustic metamaterial with negative effective mass density. *New J Phys* 2009;11:013003.
- Mead D. A general theory of harmonic wave propagation in linear periodic systems with multiple coupling. *J Sound Vib* 1973;27:235–60.
- Mead D, Parthan S. Free wave propagation in two-dimensional periodic plates. *J Sound Vib* 1979;64:325–48.
- Mead D, Pujara K. Space-harmonic analysis of periodically supported beams: response to convected random loading. *J Sound Vib* 1971;14:525–41.
- Mead DJ. Free wave propagation in periodically supported, infinite beams. *J Sound Vib* 1970;11:181–97.
- Mead DJ. Wave propagation and natural modes in periodic systems: I. Mono-coupled systems. *J Sound Vib* 1975;40:1–18.
- Y.K. Lin, T. McDaniel, *Dynamics of beam-type periodic structures*, (1969).
- Mead DJ. A new method of analyzing wave propagation in periodic structures; applications to periodic Timoshenko beams and stiffened plates. *J Sound Vib* 1986; 104:9–27.
- Orris RM, Petyt M. A finite element study of harmonic wave propagation in periodic structures. *J Sound Vib* 1974;33:223–36.
- Axmman W, Kuchment P. An efficient finite element method for computing spectra of photonic and acoustic band-gap materials: I. Scalar case. *J Comput Phys* 1999; 150:468–81.
- Åberg M, Gudmundson P. The usage of standard finite element codes for computation of dispersion relations in materials with periodic microstructure. *J Acoust Soc Am* 1997;102:2007–13.

- [56] Sorokin S, Broberg P, Steffensen M, Ledet L. Finite element modal analysis of wave propagation in homogeneous and periodic waveguides. *Int J Mech Sci* 2022;227:107444.
- [57] Dal Poggetto VF, Serpa AL. Elastic wave band gaps in a three-dimensional periodic metamaterial using the plane wave expansion method. *Int J Mech Sci* 2020;184:105841.
- [58] Xie L, Xia B, Liu J, Huang G, Lei J. An improved fast plane wave expansion method for topology optimization of phononic crystals. *Int J Mech Sci* 2017;120:171–81.
- [59] Guarín-Zapata NG. Evaluation of the spectral finite element method with the theory of phononic crystals. *J Comput Acoust* 2015:23.
- [60] Gopalakrishnan S, Doyle J. Spectral super-elements for wave propagation in structures with local non-uniformities. *Comput Meth Appl Mech Eng* 1995;121:77–90.
- [61] Nobili A, Erbaş B, Signorini C. Veering of Rayleigh–Lamb waves in orthorhombic materials. *Math Mech Solids* 2022;27:1783–99.
- [62] Achaoui Y, Khelif A, Benchabane S, Laude V. Polarization state and level repulsion in two-dimensional phononic crystals and waveguides in the presence of material anisotropy. *J Phys D Appl Phys* 2010;43:185401.
- [63] Chen JT, Hong HK, Yeh CS. Modal reaction method for modal participation factors in support motion problems. *Commun Numer Methods Eng* 1995;11(6):479–90.
- [64] Nieto M, Elsayed M, Walch D. Modal participation factors and their potential applications in aerospace: a review. In: *Proceedings of the Canadian society for mechanical engineering international congress*, May 27-30; 2018.
- [65] Ruzzene M, Scarpa F, Soranna F. Wave beaming effects in two-dimensional cellular structures. *Smart Mater Struct* 2003;12.
- [66] Phani AS, Woodhouse J, Fleck NA. Wave propagation in two-dimensional periodic lattices. *J Acoust Soc Am* 2006;119:1995–2005.
- [67] Perkins N, Mote Jr C. Comments on curve veering in eigenvalue problems. *J Sound Vib* 1986;106:451–63.
- [68] Veletsos AS, Ventura CE. Modal analysis of non-classically damped linear systems. *Earthq Eng Struct Dyn* 1986;14(2):217–43.
- [69] Füllekrug U. Determination of effective masses and modal masses from base-driven tests. In: ; 1996. 14 th.
- [70] Aenlle M, Juul M, Brincker R. Modal mass and length of mode shapes in structural dynamics. *Shock Vib* 2020;2020.
- [71] Noor AK, Peters JM, Min BJ. Mixed finite element models for free vibrations of thin-walled beams. *Finite Elem Anal Des* 1989;5:291–305.